THESIS

DEVELOPMENT, TESTING, AND VALIDATION OF A HEAT TRANSFER MODEL FOR BI-PROPELLANT LIQUID ROCKET ENGINES

Submitted by

Jadon A. Roberts

Department of Mechanical Engineering

In partial fulfillment of the requirements

For the Degree of Master of Science

Colorado State University

Fort Collins, Colorado

Fall 2024

Master's Committee:

Advisor: Bret Windom

Dan Wise
Jim Adams

ABSTRACT

DEVELOPMENT, TESTING, AND VALIDATION OF A HEAT TRANSFER MODEL FOR BI-PROPELLANT LIQUID ROCKET ENGINES

Accurately modeling the heat transfer characteristics in a bi-propellant liquid rocket engine is a time and resource intensive process. The highly unpredictable and turbulent nature of the combustion requires complex modeling to predict the temperatures and fluid properties. These properties are required to evaluate material requirements and thermal performance. The primary objective of this project was to determine the effectiveness of an adaptable analytical heat transfer model implemented in MATLAB. The analytical model was pursued for the dramatic speed increase over numerical techniques such as computational fluid dynamics (CFD). The effectiveness of the model is determined by comparing results to CFD simulations as well as data obtained from testing. Strong correlations can be drawn with variations a low at 1% between the CFD and analytical models. Three separate engines were analyzed to gauge the effectiveness of the analytical model across various engine and cooling configurations. A 10 N, 250 N and 2.9 kN thrust engines were developed. Extensive analysis was done on all engines using both the analytical model and CFD. These engines were designed with a wide range of cooling methods including radiative, ablative and regenerative cooling. A test stand previously only capable of testing hybrid rocket engines, was modified to allow for the testing of liquid bi-propellant rocket engines. The needed modifications included the addition of a fuel tank with mass measurement, venting and control valves, and fuel line sensing equipment. Upgrades were completed on the data acquisition system to incorporate additional sensors and controls. Further work was done to improve the safety of the test stand through redundancy and automation. These modifications culminated in two successful static fires of the 2.9 kN engine. The predicted temperatures of the 2.9 kN engine were compared to the test results from the static fires.

TABLE OF CONTENTS

LIST OF TABLES

LIST OF FIGURES

Chapter 1

Introduction

The continual development of novel rocket engines are crucial to the growth of the space industry. Inexpensive and reliable propulsion is needed to allow for the reduction of cost to lift vehicles, satellite positioning and deep space probes. Rocket engines generate thrust from high pressure combustion of a fuel and oxidizer. As such they operate under extreme thermal and structural conditions. The theory behind rocket engine performance (covered in detail in Chapter 2) correlates the operating efficiency of the engine with the combustion temperature and pressure. The higher temperature and pressure an engine can operate at, the higher the engine efficiency. Accurate modeling methods are needed during the design phase of new engines to achieve the highest efficiency, thus reducing costs.

1.1 Types of Rocket Engines

Two types of engines are in use in the commercial space sector currently to provide propulsion services. Solid rocket motors consist of a powder oxidizer and fuel suspended in a binder material to create solid propellant. Due to the solid form of the propellant, solid motors can be stored at ambient conditions often for indefinite amounts of time. Solid motors can be designed such that significant ignition energy is required for ignition providing safety until used. This is ideal in situations where personnel are required to handle and transport motors. Solid motors however once ignited cannot be shut down until all propellant has been burned. In addition they cannot be throttled to vary the amount of thrust produced. Solid rockets utilize insulation to prevent material failure due to high temperatures. The insulation is sufficient because of the short burn times of solid rocket engines.

Liquid rocket engines in contrast use liquid propellants for both the fuel and oxidizer and often operate for much longer periods. The combustion temperature of rockets can reach in excess of $6,000°$F ($3,300°$C). These temperatures are far above the melting temperature of metals thus

requiring more advanced cooling methods of the combustion chamber. Three common methods being regenerative cooling, radiative cooling and ablative cooling. Regenerative cooling is implemented by running liquid propellant through small channels in the combustion chamber wall before injection into the combustion chamber. Heat is transferred from the combustion chamber wall into the propellant simultaneously cooling the combustion chamber and heating the propellants. Radiative and ablative cooling are explained in detail in Chapter 2. The benefits of using liquid rockets most notably are the the ability to throttle the engine and the ability to shut down and restart the engine an indefinite amount of times.

While liquids overcome the shortcomings of solid motors in operation, the propellants used in liquid engines can provide significant safety and logistic issues. Liquid Oxygen is the most common oxidizer used. Due to the cryogenic temperatures required to keep oxygen in the liquid phase extensive support equipment is required for storage. Additionally, fuels like hydrogen and methane also require cryogenic conditions. These oxidizers and fuels work well for launch vehicles where ground equipment can maintain the temperature until launch, however engines with prolonged operation in space cannot maintain the temperature required for these propellants. Traditionally liquid rocket engines designed for prolonged in-space operation use fuels categorized as hypergolics.

Hypergolic propellants are propellant combinations that will spontaneously ignite when the are mixed. All commonly used hypergolics can be stored as a liquid at room temperature, thus solving the cryogenic problem seen with oxygen and other fuels. Hypergolics are however extremely toxic and corrosive increasing the safety and operational concerns discussed above.

1.2 Project Background

This research sought to solve these issues by modeling heat transfer characteristics of several engines with non toxic, storable propellants. Three liquid engines were designed and analyzed: a 2.2 pound-force (lbf), a 56 lbf, and a 650 lbf thrust engine. The 2.2 lbf and 56 lbf engines utilized a 50/50 mix of ethane and ethylene for the fuel and nitrous oxide for the oxidizer. These

propellants while not toxic, can also be indefinitely stored in the liquid phase. Additionally both propellants exhibit the same vapor pressure meaning they can be self-pressurized in a common bulkhead configuration.

The 2.2 lbf engine referred to as the Reaction Control System Thruster (RCST) utilizes radiative cooling to dissipate the minimal heat generated. The 56 lbf engine was designed for the same vehicle in order to share propellant tanks with the RCST. The Regeneratively Cooled Main Propulsion Engine (RCMPE), as the name suggests, is cooled via regenerative cooling channels in the combustion chamber. The large 650 lbf engine, designated as the Ablatively Cooled Main Propulsion Engine (ACMPE), utilizes the same oxidizer with ethanol used as the fuel. Unlike the RCST and RCMPE, the ACMPE is not designed for steady state operation instead using an ablative liner for the short ten-second maximum burn time.

Several challenges were identified during the design phase that necessitated a fast, accurate, heat transfer model. As the propellant is designed to operate in a self-pressurized system, the propellants can be stored very near their vapor pressures. A pressure drop is expected as the propellants flow through the small cooling channels. The propellant will also experience significant heating due to the transfer of heat from the combustion chamber. Both these factors make phase change of the propellants in the channels likely. Extensive work has been done to determine the effects of boiling inside coolant channels.

Specifically, Trejo et al. studied the effects boiling has on liquid methane inside cooling channels in regenertively cooled rocket engines. It was found that the propellant performed well as a coolant until fully boiled inside the coolant channel. Significant cooling capacity was lost once the coolant was fully in the gaseous state [1]. Both the oxidizer and fuel were used as coolant in the RCMPE in order to combat this issue. The additional cooling capacity along with minimizing the pressure drop was expected to prevent boiling in the coolant channels.

1.3 Literature Review

While numerous research papers have been published on modeling a regeneratively cooled rocket engine using a single propellant as coolant, little work was found where both fuel and oxidizer were used as coolant. Naraghi et al. explored using both oxidizer and fuel as coolants in a dual regenerative cooling circuit. This circuit had both oxidizer and fuel injected at the highest heat flux zone, the throat, with one of the propellants flowing downstream towards the exit of the nozzle and the other flowing upstream towards the injector. This provided high cooling capacity with both coolants being at the lowest temperature at the area of highest heat flux. The propellant flowed through the coolant channels downstream proved difficult to recover and was typically dumped. Due to the need to carry additional mass that was unused in the combustion chamber this system was very inefficient [2]. While the work of Naraghi use both the fuel and oxidizer as coolant it varies significantly from the work outlined in this thesis. The RCMPE injects the coolants at the downstream end of the engine and flows the propellants the full length of the combustion chamber.

In 2020 Browne conducted analytical and Computational Fluid Dynamic (CFD) modeling for a 900 lbf thrust regenertively cooled liquid rocket engine. This engine used the same propellant combination of ethane/ethylene and nitrous oxide and used both as coolant. The higher thrust of this engine allowed for larger flow rates which allowed for greater cooling capacity. Additionally at the $1,000$ PSI operating pressure the fuel and oxidizer used would require additional pressurization from an inert gas system of a pump. This allowed for a significantly larger margin before the propellants would change phase. Promising results were seen between the analytical and CFD analysis performed on this engine [3]. Browne's methods and results were used as a framework when approaching the work outlined in this thesis.

1.4 Project Scope

With the tighter temperature and pressure tolerances to remain a liquid in the RCMPE, greater accuracy is required than obtained by Browne. By replacing the general combustion process and convection correlations used in Brownes analytical model with more representative combustion

properties and specific convection correlations, the model accuracy was predicted to be increased. Additionally by conducting the CFD work in *Converge CFD* the model could be run faster and with higher confidence than the CFD tools used by Browne.

By adding additional precision and capabilities the analytical model will become an invaluable tool in liquid rocket engine design. The main benefit of the analytical model to numerical models such as CFD is the solution time. CFD often takes days to weeks to solve a complex heat transfer system. The analytical model however is solved in a matter of seconds. This allows for extremely fast iteration of engine designs before manufacturing. Additionally the model can be designed in a way to allow for a wide range of engine geometries and cooling methods. The three engines studied were chosen for their representative range of not only physical size, but also for the cooling methods used for each engine. No existing work was found studying the effectiveness of a heat transfer model capable of predicting performance in such a wide range of engines.

Lacking from many of the published works are real-world engine tests validating these heat transfer models. Testing of all three engines was planned using a mobile test stand at Colorado State University. The test stand required the addition and validation of a fuel delivery system with a static fire of the ACMPE used to confirm functionality.

This paper first explores the fundamental principles behind rocket engines. Also explored are various configurations commonly used when designing liquid rocket engines and their cooling systems. Detailed explanations are then presented for the analytical model and how each of the three engines studied were setup and solved. The CFD simulation is then thoroughly described. Chapter 3 concludes with the work completed on the test stand to obtain a static fire of the ACMPE. Chapter 4 presents the results from the analytical models as well as the CFD simulations. These results are compared for the RCMPE to gauge model effectiveness. Static fire data is presented and the key features of the stand validation are highlighted. This paper ends with a road map for continuing the work of model validation.

Chapter 2

Background

2.1 General Rocket Theory

At its simplest form a rocket engine leverages high temperature and pressure combustion products to produce thrust. This is accomplished by exchanging the relatively slow moving combustion products and accelerating the flow through a converging diverging nozzle. Figure 2.1 shows the typical layout of a liquid rocket engine. The thrust produced is directly proportional to the mass flow rate of the combustion products and its speed as it leaves the nozzle (Eqn. 2.1).

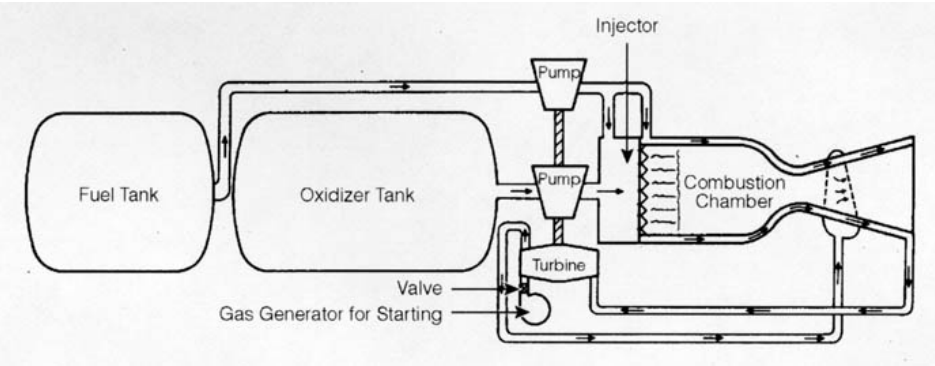

Figure 2.1: Typical configuration of a Liquid rocket engine and support equipment [4]

Several methods are employed to determine the efficiency of rocket engines. The specific impulse (ISP) is used as an overall efficiency of the entire engine including combustion chamber and nozzle performance. ISP can be defined as the ratio of thrust to the weight flow of propellants for an engine. This can be seen in Equation 2.2, where $\dot{W}$ represents the weight flow rate of both propellants. The units of ISP are given in seconds and typically range from 200-500 seconds [5].

$$F = mV_e \tag{2.1}$$

$$ISP = \frac{F}{\dot{W}} \tag{2.2}$$

The performance of a rocket engine can be further divided by the efficiencies of the combustion chamber and nozzle. The characteristic velocity (C^*) can be defined as the required amount of propellant burned in order to maintain the required nozzle stagnation pressure [6]. C^* is a strong indicator for the design quality of the injector and combustion chamber. It can be found empirically in Equation 2.3 where $(P_c)_{ns}$ is the nozzle stagnation pressure, A_t is the area of the throat and g represents the gravitational constant. Alternatively, the theoretical C^* can be found using thermodynamic properties of the exhaust gas at the nozzle inlet. This is seen in Equation 2.4, where γ is the specific heat ratio, R is the gas constant and $(T_c)_{ns}$ is the stagnation temperature.

$$C^* = \frac{(P_c)_{ns} A_t g}{\dot{W}} \tag{2.3}$$

$$C^* = \frac{\sqrt{g\gamma R(T_c)_{ns}}}{\gamma\sqrt{\left[\frac{2}{\gamma+1}\right]}} \tag{2.4}$$

The performance of the converging-diverging nozzle can be expressed by the thrust coefficient (C_f). As with C^* two equations can be used to find the design quality of the nozzle. From empirical values, C_f can be expressed in Equation 2.5. The theoretical C_f can also be found using the exhaust gas properties as well as the nozzle exit pressure (P_e), the ambient pressure outside the nozzle (P_a) and the nozzle area expansion ratio (ϵ). This is seen in Equation 2.6.

$$C_f = \frac{F}{A_t (P_c)_{ns}} \tag{2.5}$$

$$C_f = \sqrt{\frac{2\gamma^2}{\gamma-1}\left[\frac{2}{\gamma+1}\right]^{\frac{\gamma+1}{\gamma-1}}\left[1-\left(\frac{P_e}{(P_c)_{ns}}\right)^{\frac{\gamma-1}{\gamma}}\right]} + \epsilon\left[\frac{P_e - P_a}{(P_c)_{ns}}\right] \tag{2.6}$$

For all the above equations the stagnation pressure can be found given the injector pressure (P_i), the molecular weight at the injector (M_i), as well as other thermodynamic properties. This is seen in Equation 2.7. Similarly the stagnation temperature can be found from the injector temperature (T_i), seen in Equation 2.8.

$$(P_c)_{ns} = P_i\Big[1 + \frac{1}{2}(\gamma - 1)M_i^2\Big]^{\frac{\gamma}{\gamma-1}} \tag{2.7}$$

$$(T_c)_{ns} = T_i\Big[1 + \frac{1}{2}(\gamma - 1)M_i^2\Big] \tag{2.8}$$

The converging-diverging nozzle can be designed in such a way that flow is accelerated through the entire length. The gas is assumed to be isentropic and the flow rate is constant. It can also be assumed that the entire length of the nozzle falls under compressible flow as the Mach number (Ma) is greater than 0.3. The high pressure gas from the combustion chamber first flows into the converging section. As the cross sectional area decreases the velocity is increased while the pressure decreases. At the throat the exhaust gas reaches $Ma = 1$ and is now considered sonic flow. Using the conservation of mass the following relationship can be found where V is the exhaust velocity and A is the cross sectional area of the nozzle [7].

$$(1 - Ma^2)\frac{dV}{V} = -\frac{dA}{A} \tag{2.9}$$

From this equation it can be seen that the exhaust velocity's relationship with the cross sectional area is dependant on the value of Ma. For $Ma < 1$ a decrease in area produces an increase in velocity. For $Ma > 1$ a increase in area directly relates to an increase in velocity. Based on this relationship the ideal nozzle is designed to accelerate the sub-sonic flow to exactly $Ma = 1$ before accelerating it further in the diverging section.

The needed area of the throat to achieve chocked flow can be found by solving for A_t in Equation 2.3. The cross sectional area of the nozzle exit (A_e) can then be found using Equation 2.10.

$$\epsilon = \frac{A_e}{A_t} = \frac{\left(\frac{2}{\gamma+1}\right)^{\frac{1}{\gamma-1}} \left[\frac{(P_c)_{ns}}{Pe}\right]^{\frac{1}{\gamma}}}{\sqrt{\frac{\gamma+1}{\gamma-1}\left[1-\left(\frac{P_e}{(P_c)_{ns}}\right)^{\frac{\gamma-1}{\gamma}}\right]}} \tag{2.10}$$

When designing the combustion chamber the total volume is a key parameter. The propellants must have sufficient volume to completely combust during transit of the engine. If the chamber is undersized this 'stay time' will be insufficient and the engine will suffer efficiency losses and the propellants are not fully consumed. Additionally a volume that is too large adds unnecessary weight to the system. The characteristic length (L^*) can be used to determine the ideal volume (V_c) for a combustion chamber (Eqn. 2.11).

$$L^* = \frac{V_c}{A_t} \tag{2.11}$$

The L^* parameter is derived from experimental data. This value can change dramatically by injector design, propellant combination and thrust requirements. For new design it is recommended to start from published results of engines of similar size and propellants. Through testing this L^* value can be refined. All equations above derived from *Modern Engineering for Design of Liquid-Propellant Rocket Engines* [6].

2.2 Injector Design

All types of rocket engines, whether solid, hybrid or liquid fueled, include both fuel and oxidizer. This paper focuses solely on the operation of liquid fueled rocket engines. Liquid fueled rocket engines provide many benefits over other designs namely the ability to throttle and the

reusability. At the heart of this is the injector. The injector has the single greatest impact on engine stability, reliability and efficiency.

The injector is responsible for atomization of both the fuel and oxidizer as well as ensuring a well mixed spray of propellants before ignition. In pressure fed systems the injector is often used to directly control the mass flow rates of propellants into the combustion chamber.

Many types of injectors have been well proven in the past. Three common designs are the impingement, pintle and swirl injectors. Impingments injectors are the simplest. The fuel and oxidizer are injected at a colliding angle. When the two high pressure streams collide, the atomization and mixing is accomplished. Figure 2.2 shows doublet and triplet, (unlike impingement) as well as self-impinging (like impingment) configurations of injectors.

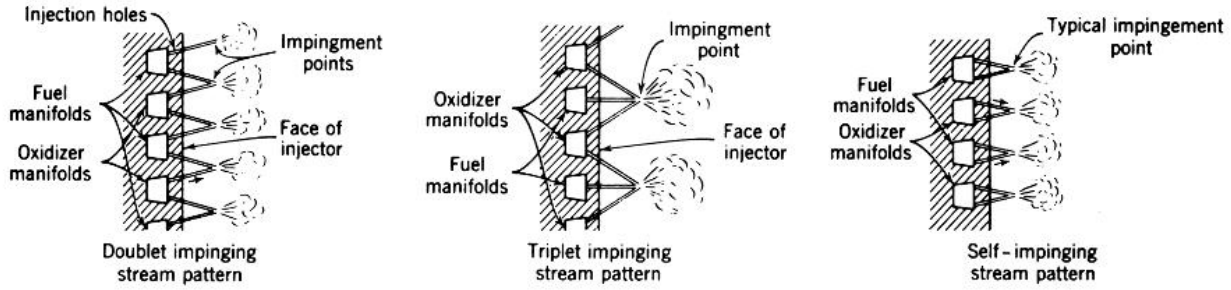

Figure 2.2: Doublet, triplet and self-impinging configurations of liquid impingement injectors [6]

Unlike doublets and triplets, while very easy to manufacture, they often suffer from poor mixing. The much greater flow rates of oxidizer present in most engines greats a mismatch of flow of the two streams thus causing biased patterns. Theses injectors also create a mostly 2D dimensional fan upon collision. This can cause hot spots in the combustion chamber. Finally these types of injectors are prone to interference from the combustion process as it can distort the injection pattern.

Pintle injectors (also referred to as coaxial injectors) are a family of designs that utilize coaxial flow of the oxidizer and fuel. In pure coaxial injectors the outer concentric stream is flowed at a drastically different velocity as the inner stream. This introduces a strong shear gradient allowing

for high efficiency mixing. Other designs as seen in Figure 2.3, use angled deflectors to increase the mixing and produce the ideal cone shape of mixed propellants. Pintle injectors are well proven to provide stable combustion especially in designs where the oxidizer is liquid and the fuel is vaporized exiting the injector.

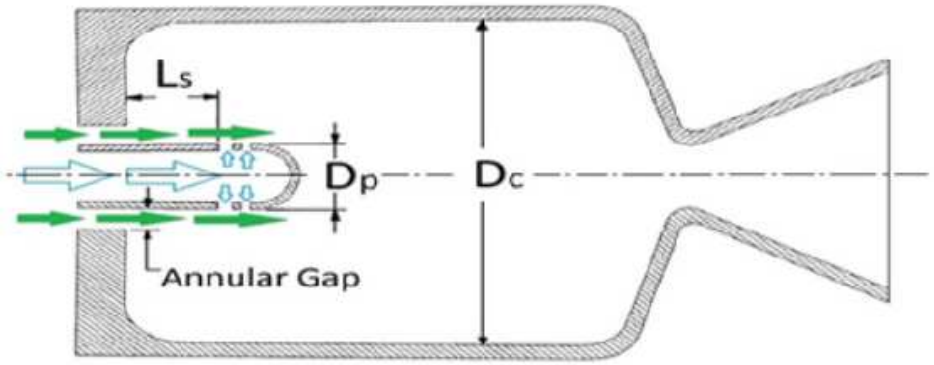

Figure 2.3: Common pintle injector cross section [8]

Swirl injectors operate very similar to coaxial injectors but with the key difference that both propellants are flowed into the injector assembly tangentially. This imparts a strong rotational movement to the fluid and upon exit of the injector spreads the flow in the desired cone shape. This added rotation provides additional shear gradients that improves the mixing ability of the propellants. The added mixing efficiency as stated earlier is a key parameter in the combustion stability and engine efficiency. A typical configuration can be seen in Figure 2.4.

2.3 Liquid Rocket Cooling Methods

One of the main issues with operating a liquid rocket engine is heat management. The high combustion temperatures combined with the strict weight budget on rocket engines provides many challenges for designing an effective cooling solution. No one correct method for cooling a rocket engine exists. Each method can sufficiently cool a certain engine configuration while under performing on a different engine. Most engines in production utilize a combination of cooling methods for best results.

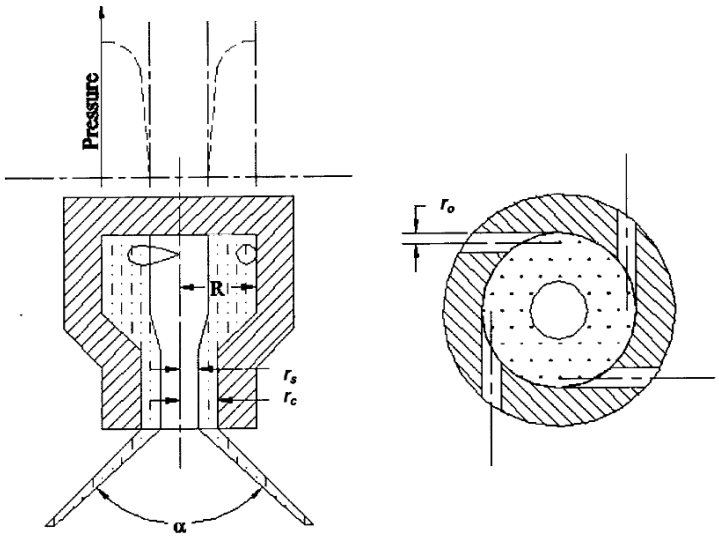

Figure 2.4: A common swirl injector configuration with the side view cross section (left) and top view (right) [9]

The simplest solution involves cooling through pure radiation from the outside surface of the combustion chamber and nozzle. This methods works primarily well on small engines with very short intermediate burn regimes. The small size of these engines require minimal cooling capacity and are often implemented in vacuum environments where the radiation mode of heat transfer is particularly efficient.

This simple form of passive cooling is primarily employed in reaction control thrusters for small (< 26.69 N engines operating in vacuum. The simplicity is a key factor in the minimal weight and size of these engines. This heat rejection can be seen in the vacuum test hot fire of Agile Space's A110 engine (Fig. 2.5). The main disadvantage to radiatively cooling engines is the limited cooling capacity. These engines are restricted to short burn times with cooling periods between.

Another very simple method for cooling the combustion chamber is film cooling. Film cooling can be accomplished by injecting excess fuel near the inner combustion chamber wall. This provides a fuel rich combustion region where the combustion temperatures are substantially less than the center of the chamber. Fuel can also be injected directly onto the surface of the chamber wall providing a cooling effect as it evaporates. Film cooling can greatly reduce the combustion

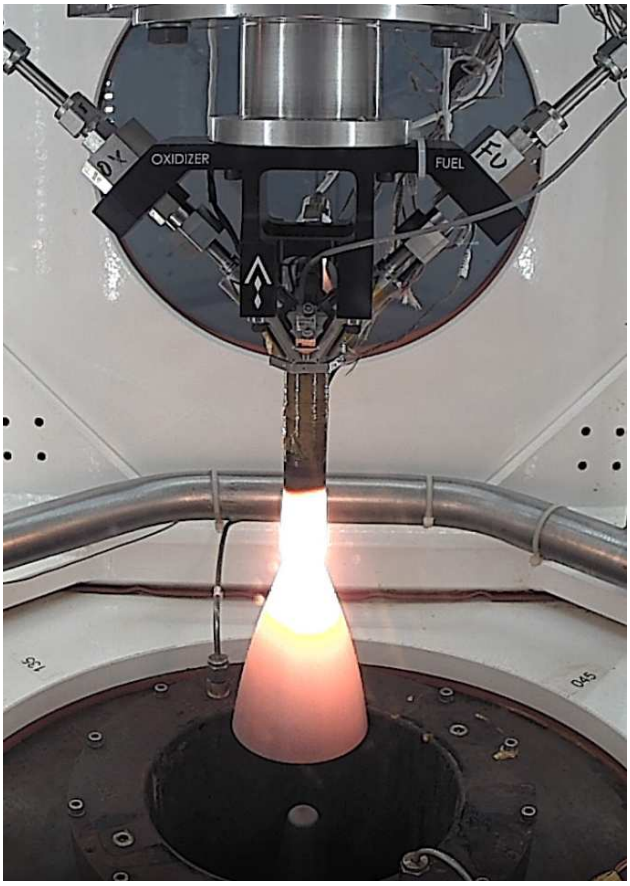

Figure 2.5: Agile Space's A110 rejecting heat via radiation in a vacuum chamber hot fire test [10]

chamber wall temperatures on engines of all sizes. The main drawback to film cooling is engine efficiency and complexity. By creating fuel rich areas in the combustion chamber the ideal fuel to oxidizer ratio is changed impacting the efficiency of the combustion. Furthermore film cooling is very hard to utilize uniformly. It is relatively simple to add additional fuel injectors at the top of the engines, however the cooling benefits of these will diminish further away from the top. As the fuel is evaporated from the surface, injectors are needed along the entire chamber and nozzle to replace the fuel layer. For this reason it is very rare to see an engine cooled solely by film cooling.

Ablative cooling is used as a simple, relatively low cost but very effective form of cooling. An ablative surface when contacted by the hot gas of the combustion will begin the process of pyrolysis. That is the resins will begin to break down to a char while off gassing volatile products into the combustion stream. This char layer can provide very effective insulation before breaking down

and joining the combustion stream. As this process is inherently destructive ablative materials are not reusable. Common ablative materials include phenolic-resin impregnated into a high silica material and carbon-carbon composites. Due to the lack of reusability this method of cooling is typically reserved for single mission or single burn engines. This method is also often constrained to designs under 20.6 bar (300 PSI) as the chamber pressure has a direct relationship to the speed of ablation.

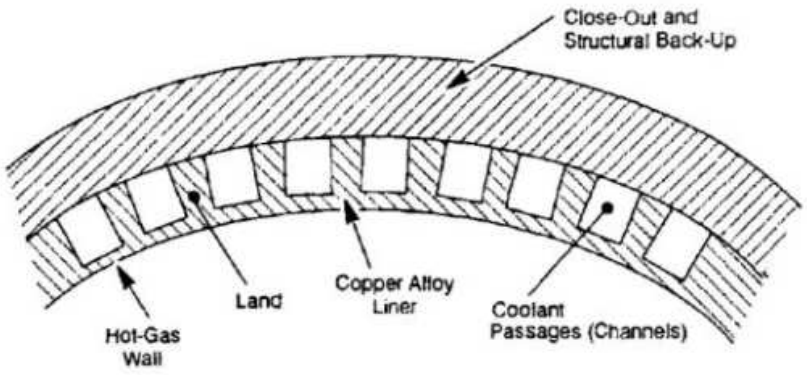

Figure 2.6: Combustion chamber wall with cooling channels [6]

The most effective form of active cooling in liquid rocket engines is regenerative cooling. This is by far the most commonly used cooling method for production engines. Before injection, one or both the propellants are flowed along channels in the combustion chamber wall. For larger engines utilizing hydrocarbon fuels, the fuel is preferred for its high specific heat. Using regenerative cooling on smaller engines is often more difficult as the flow rates of the propellants are greatly reduced. For these engines the oxidizer can be flown in addition to the fuel for added cooling capacity. A representative chamber wall design can be seen in Figure 2.6.

Before additive manufacturing become a viable option designing and manufacturing a regeneratively cooled rocket engine was done at great expense. Many factors still make the design of these engines very difficult. The number of coolant channels is maximized to increase the available surface area for heat transfer. This results is very small channels and depending on the propellant type, significant pressure loss can be experienced in the cooling channels. If significant pressure

loss is seen combined with the increase in temperature experienced, the propellants risk changing phase. This can be very destructive to an engine and the injector.

The benefits of this cooling method far outweigh the design challenges. This cooling method provides indefinite firing time while not decreasing engine efficiency at all. The heat that is removed from the system is transferred to the propellants before being injected back into the system. This system is also very lightweight and requires very few moving parts. For these reasons regeneratively cooled rocket engines have become the standard.

Chapter 3

Methodology

3.1 Engine Design

The design for all three engines studied followed the same path. The initial requirements were first set. These included thrust, target chamber pressure, fuel, oxidizer and the fuel to oxidizer ratio. Many of these requirements were set out by project sponsors while others were chosen based on previous experience and convenience to the design. The National Aeronautics and Space Administration (NASA) Chemical Equilibrium Application (CEA) code was used to solve for key engine parameters [11]. The NASA CEA code is a tool published by NASA for analyzing the performance of engines with input variables such as engine pressure, fuel combinations, oxidizer to fuel ratio and area ratios.

In order to find the nozzle area ratio for the set thrust, Equation 2.10 is used. Since the area ratio is a required input variable for NASA CEA, the ratio of specific heats is first estimated. This area ratio is input into NASA CEA and the specific heat ratio solved for is used to refine the area ratio before being solved again. This process is repeated until convergence is seen in the specific heat ratio output.

Once provided with each engines C^*, ISP, and C_f, Equations 2.3 and 2.5 can be used to find the propellant mass flow rate and area of throat respectively. The area of the throat, nozzle area ratio and L^* dictate combustion chamber and nozzle dimensions. Injector orifices were then sized based on Equation 3.1 [12]. The discharge coefficient (C_D) was assumed to be 0.6 and verified through testing.

$$A = \frac{\dot{m}}{C_D(\sqrt{2p\Delta P}} \tag{3.1}$$

Given the above parameters the RCST was designed to be manufactured in house. The exploded view of the RCST model can be seen in Figure 3.1. The design includes two main com-

ponenets, a combustion chamber and an injector plate. These two components are connected via 4 1/4-20 bolts and are sealed with two high temperature Viton® o-rings.

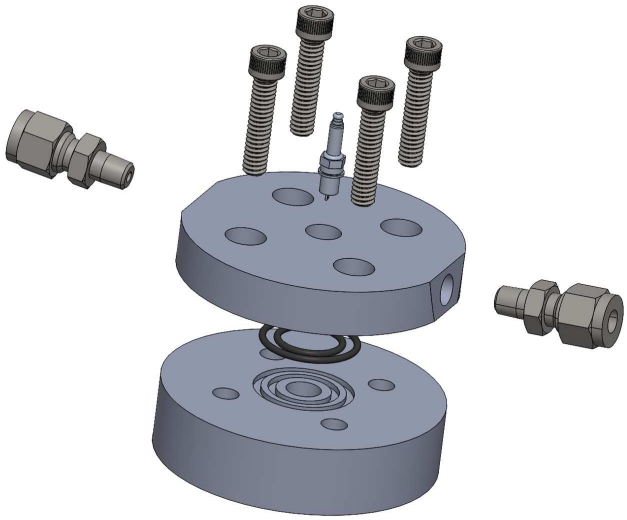

Figure 3.1: Exploded view of RCST CAD model

Ignition is provided by a miniaturized spark plug centered above the location of propellant mixing. The unlike doublet designed for this engine can be seen in the cross section in Figure 3.2. The engine was manufactured out of Titanium in order to handle the high temperatures of the combustion chamber and nozzle. The overall large diameter of the engine compared to the small diameter of the combustion chamber serves several purposes. Most importantly the large surface area increases the amount of heat dissipated by radiation which decreases the overall temperature of the engine. The large diameter also allows the use of Swagelok® fittings allowing for more reliable and faster testing.

The RCMPE was designed and manufactured by project partners at Pioneer Astronautics, but extensive analysis was done by by CSU to aid in the design. The main design consisted of a outer shell with oxidizer and fuel channels going from a plenum at the nozzle end of the engine to the radial injector holes at the top of the engine. This configuration can be seen in Figure 3.3. A solid piece graphite liner and nozzle were placed on the inside of the cooling shell. The top of the combustion chamber was capped with a spark plug providing a ignition source.

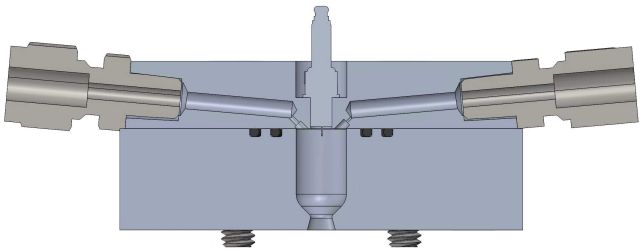

Figure 3.2: Cross section of RCST CAD model

Figure 3.3: Cross section of fuel plenum and channel on the RCMPE model

The ACMPE was designed for shorter burn times than the RCMPE while providing much greater thrust at a higher chamber pressure. This engine utilizes a simple pintle injector to control flow rates and provide mixing. Figure 3.4 shows the flow of oxidizer and fuel as they enter the combustion chamber.

While no active cooling methods are employed in this engine a large amount of ablative material is used in the form of an ablative liner. This liner is constructed from a 1/4 inch fiberglass sheet infused with phenolic resin. This liner allows the ACMPE to operate for up to 30 seconds of burn time. The graphite nozzle is expected to ablate as well but at a much slower rate [13].

The nozzle and injector are secured inside the combustion chamber with retaining rings. Sealing is provided by two high temperature Viton® o-rings. Ignition is provided by a small 100 gram

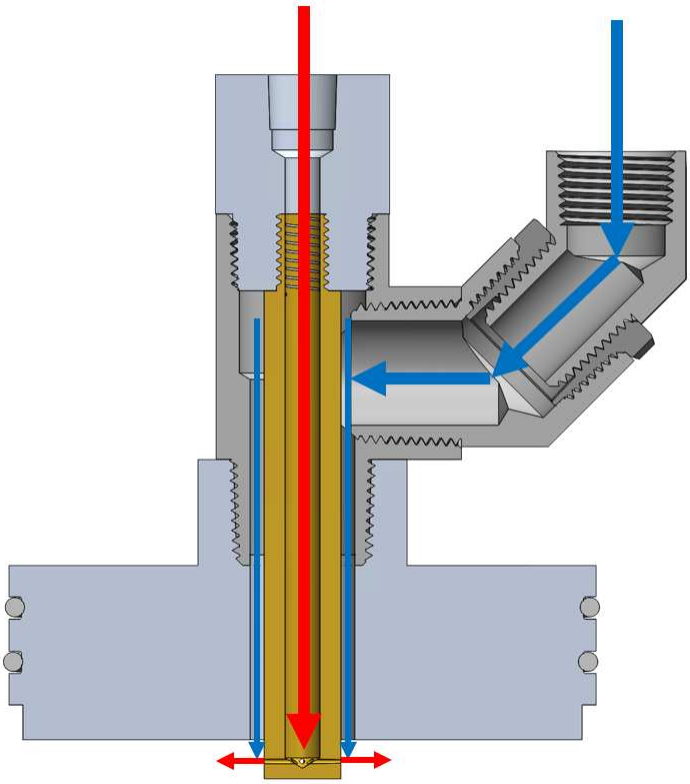

Figure 3.4: Cross section of ACMPE pintle injector. Oxidizer flow shown in blue, fuel flow shown in red

puck of solid propellant. The recipe and geometry were calibrated to provide a 10-second burn time. This pre-burner provides adequate pre-heating of the combustion chamber before the propellants are introduced. This method of ignition helps prevent hard starts caused by large amounts of propellant filling the combustion chamber before ignition. Hard starts cause a large pressure spike often causing the engine to fail.

3.2 Analytical Modeling

In order to create analytical predictions of the heat transfer key thermodynamic properties of the propellants and the exhaust gas are needed. For each engine studied the individual parameters were input into the NASA CEA code and the resulting engine performance parameters were solved. The thermodynamic properties of the exhaust gas needed are output and used in the analytical models.

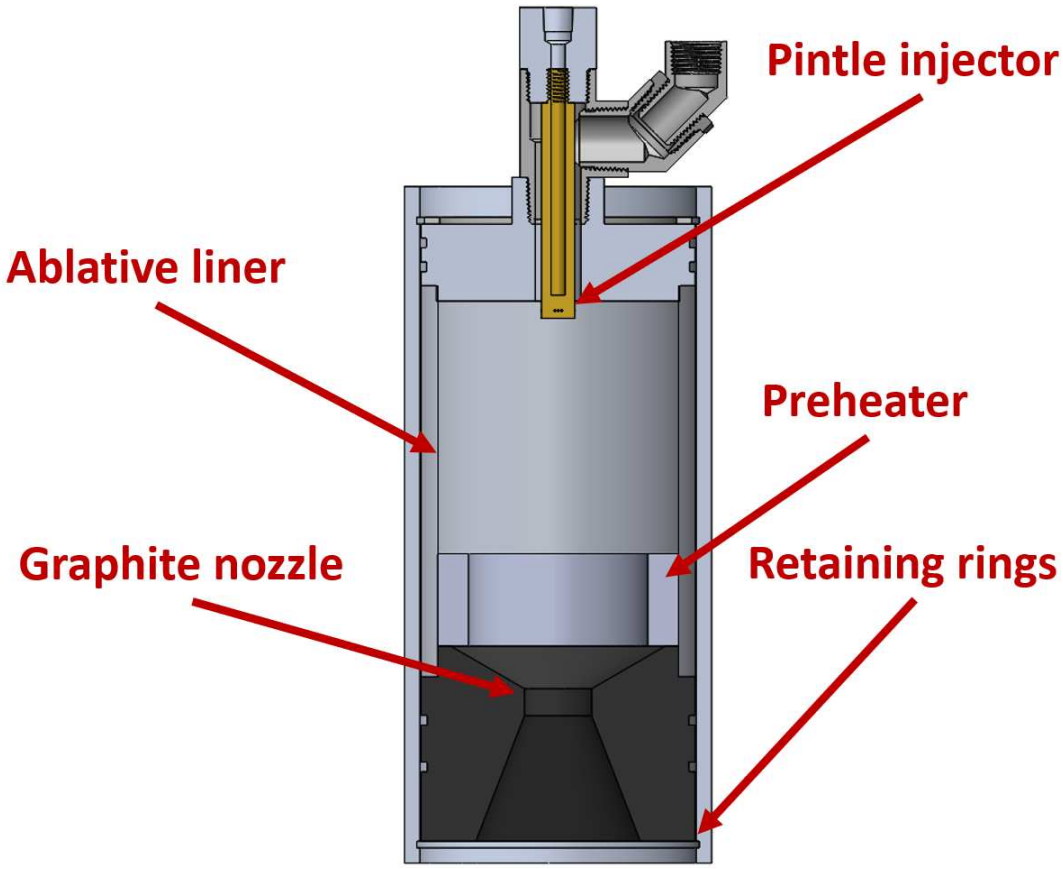

Figure 3.5: Cross section of ACMPE engine assembly

A representative table of outputs is seen in Table 3.1. The properties are output at key points along the engine, namely the chamber, throat and nozzle exit.

Table 3.1: Example CEA property output for the RCMPE engine

Property	Chamber	Throat	Exit
Temperature (K)	3253.84	3058.73	2282.90
Density (kg/m^3)	1.2516	$7.7254e-1$	1.3275e-1
Specific Heat (kJ/kgK)	4.2899	3.8242	1.8895
Ratio of Specific Heats	1.1516	1.1541	1.2209
Velocity (m/s)	1126.4	1086.9	953.9

The general strategy used for predicting the heat transfer characteristics for each engine was a resistive circuit analogy. By using this resistive circuit analysis approach a modular model capable of predicting various engine configurations can be made. Each engine can be modeled as a tube

with hot combustion gases flowing down the center. This basic model for the combustion chamber is consistent for every engine analyzed . The unique feature of each engine studied (ablative liner, regenerative channels, etc.) can be modeled by simply adding additional resistive elements in the over all circuit.

Several simplifications were made throughout the development of the analytical model to reduce computational time. This model ignores any turbulence or chemical effect of the actual combustion. It is assumed that the ignition and combustion process takes place in a relatively small volume compared to that of the combustion chamber. The combustion heat generated from the combustion chamber is modeled as hot gas with the properties from the NASA CEA solution.

This resistive circuit solution provides a 1D temperature distribution in the radial direction of the engine. A quasi-2D temperature distribution can be found by solving the 1D temperature distribution along the axial length of the combustion chamber. This methods ignores any heat transfer along the axial axis of the engine. Due to the significantly larger temperature gradients along the radial axis when compared to the axial axis this simplification should introduce minor errors.

3.2.1 Combustion Chamber

All engines studied being of similar chamber pressure and fuel properties used the same correlation for determining the heat transfer between the combustion chamber and inner chamber wall. This process was modeled as a convection resistive element. Knowing the exhaust gas velocity (V) and viscosity at three key points along the combustion chamber, these values are interpolated linearly in order to know the values at all points along the combustion chamber. It is important to note NASA CEA calculates the dynamic viscosity (μ). Where the kinematic viscosity is needed it can be found as the ratio of dynamic viscosity and the density [14]. With these interpolated property values the exhaust gas flow can be characterized using Reynolds number [15].

$$Re = \frac{VD}{\mu/\rho} \tag{3.2}$$

As expected, for all engines studied the exhaust gas flow can be considered turbulent ($Re > 10,000$) [16]. The convection coefficient can be found by using the Gnielinski correlation [17]. This correlation was chosen for its accuracy in turbulent cylindrical tube models. The Gnielinski correlation provides the Nusselt number (Nu) which can be found in Equation 3.3.

$$Nu = \frac{(f/8)(Re - 1000)Pr}{1 + 12.7\sqrt{f/8}(Pr^{2/3} - 1)} \left[1 - \left(\frac{D}{L}\right)^{2/3}\right] \left(\frac{Pr_m}{Pr_w}\right)^{0.11} \tag{3.3}$$

where

$$f = (1.82 \log_{10} Re - 1.64)^{-2} \tag{3.4}$$

Equation 3.3 can be solved for the entire length of the combustion chamber, taking into account the changing diameter and previously solved for Reynolds number. Using the thermal conductivity of the exhaust gas (k), Nusselt number and diameter the local convection coefficient (h) can be found for each descrete point along the combustion chamber.

$$h = \frac{Nuk}{D} \tag{3.5}$$

3.2.2 Reaction Control System Thruster

The radiative cooling utilized on the RCST engine requires the least resistive elements in the heat transfer model. A representative diagram of the engine model can be seen in Figure 3.6, Where Tc represents the combustion temperature and $Tsurr$ represents the temperature of the surroundings. The temperature of combustion is found using NASA CEA while the temperature of the surrounding is easily found based on the desired operating conditions. The resistive circuit analogy can be used to solve the circuit using Equations 3.6 through 3.9.

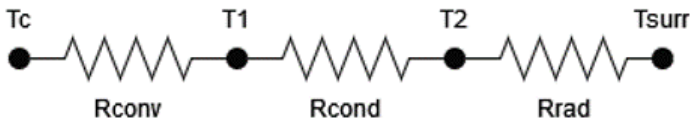

Figure 3.6: Analogous resistive circuit used for RCST model

$$q = \frac{T_c - T_{surr}}{R_{total}} \tag{3.6}$$

$$R_{cond} = \frac{\ln(r_2/r_1)}{2\pi Lk} \tag{3.7}$$

$$R_{conv} = \frac{1}{2\pi rh} \tag{3.8}$$

$$R_{rad} = \frac{T_{surf} - T_{surr}}{(\sigma\epsilon 2\pi r_2 \Delta x)(T_{suf}^4 - T_{surr}^4)} \tag{3.9}$$

The system is solved initially using a guess for the the surface temperature (T_{surf} in Equation 3.9). The total heat flux for the system is solved (Equation 3.6) and used to determine the temperature at each node in the circuit. This new value of T_{surf} is used in the next iteration and repeated until the guess and the solved value converge. Once convergence is determined, the steady state temperature of each note alone the axial length of the combustion chamber can be plotted. This provides the quasi 2D temperature distribution of the engine.

3.2.3 Ablatively Cooled Main Propulsion Engine

To model the ACMPE the same model can be used. The model requires only minor reconfiguring. The geometry variables in the model are the only things that need to be adjusted to account for the size difference. A second condutive resistive element is added between the combustion chamber and the outer wall. This element represents the ablative liner used in the ACMPE. Radiation is ignored on the outer surface as it is assumed that the natural convection will be much larger.

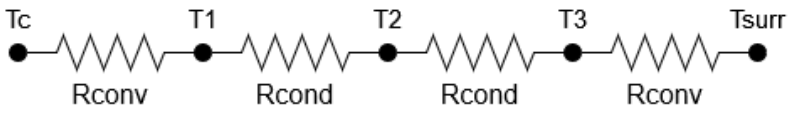

Figure 3.7: Analogous resistive circuit used for ACMPE model

The convection coefficient placed between Tc and $T1$ is calculated the same as described for the RCST model. The conduction through the liner ($T1$ to $T2$) accounts for the insulating nature of the ablative liner [18]. The outer combustion chamber is modeled again in the same ways as in the RCST model.

3.2.4 Regeneratively Cooled Main Propulsion Engine

To model the cooling capacity of the RCMPE, again a similar approach to that of the RCST was used. The modular approach to this analysis required only adding resistive elements in order to capture the added complexities of the regeneratively cooled combustion chamber. The representative circuit (Figure 3.8) represents the cooling channels in the combustion chamber wall using resistive elements in parallel.

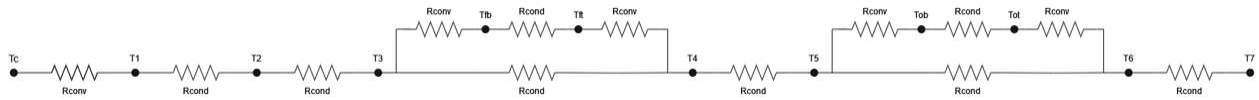

Figure 3.8: Analogous resistive circuit used for RCMPE model

Several simplifications were made in addition to the combustion simplifications outlined above. The resistive circuit analogy assumes 1D heat transfer in the radial directions. This is of particular importance when considering the coolant channels. Figure 3.9 shows an example cross section of a single coolant channel where the heat flow is labeled flowing from the combustion chamber (smaller radius) to the outside surface of the engine (larger radius). By assuming heat is only transferred in the radial directions the heat can be said to flow through the bottom of the channel, into and through the liquid and then into the top of the channel. This neglects heat transfer through the two side walls.

This assumptions allows for the heat transfer to be modeled simply as a fluid flowing between two flat plates. This geometry has been solved and simple correlations are used to determine heat transfer properties.

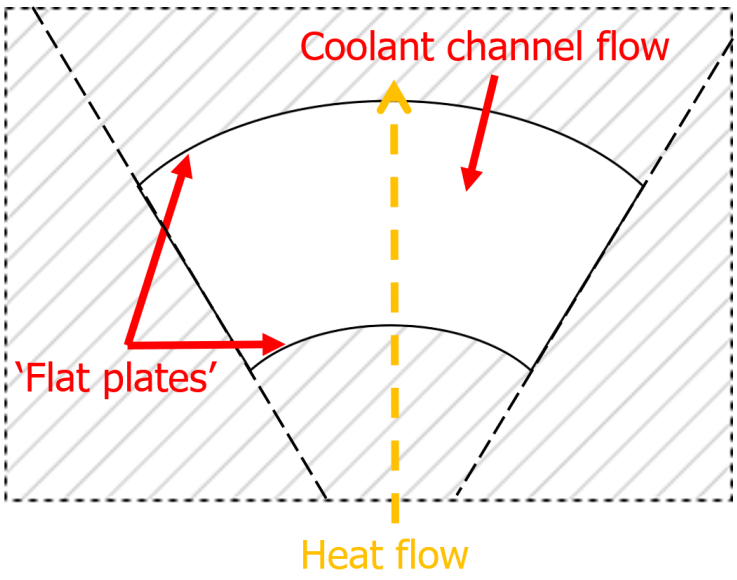

Figure 3.9: Cross section of a single coolant channel

3.3 Computational Fluid Dynamics Modeling

In order to accuratly model the RCMPE using CFD, *Converge CFD* was used. *Converge CFD* incorporates robust Conjugate Heat Transfer (CHT) capabilities for fluid to solid heat transfer solutions. *Converge CFD* was also chosen for its advanced Adaptive Mesh Refinement (AMR) engine. The small, high pressure coolant channels as well as the highly turbulent supersonic nozzle, the model requires extremely fine mesh in order to converge. The AMR allows for a course global mesh with only minor manual local mesh refinement. Through the solution process *Converge CFD* determines where a finer mesh is required and applies the needed mesh. This single feature greatly reduces the solution time for complex models such as the RCMPE.

A modified 3D geometry was imported into *Converge CFD* and the mesh was repaired and prepared using the geometry tools. All inlet and outlets were sealed and the appropriate boundary conditions were applied. The exhaust gas inlet, fuel and oxidizer channel inlet were prescribed with a fixed mass flow rate and temperature condition. The nozzle exit was defined as a pressure outflow at ambient pressure and temperature while both coolant channels were set to the combustion chamber pressure and temperature. All interfaces were set as the *Walls* boundary type with CHT enabled.

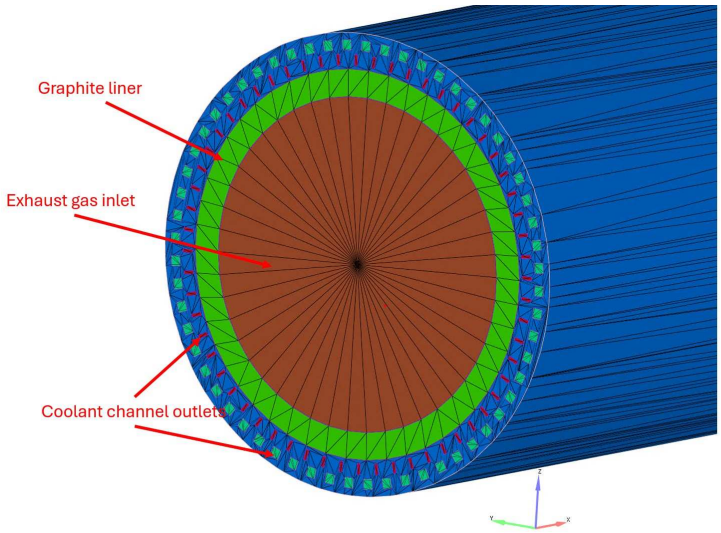

Figure 3.10: Prescribed inlet and outlet conditions for top of CFD geometry

The exhaust gas was modeled using the same composition determined from NASA CEA as the analytical model used. The *Redlich-Kwong* equation of state was used inside *Converge CFD* to determine all gas properties. The stainless steel and graphite properties were imported. As both exhibited minor property change under temperature variations, all properties were assumed constant.

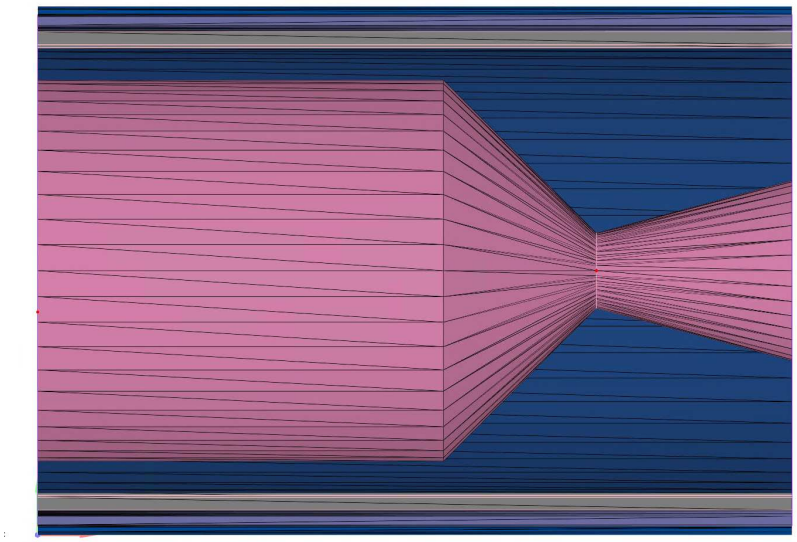

Figure 3.11: Section view of the CFD geometry showing the combustion chamber interface

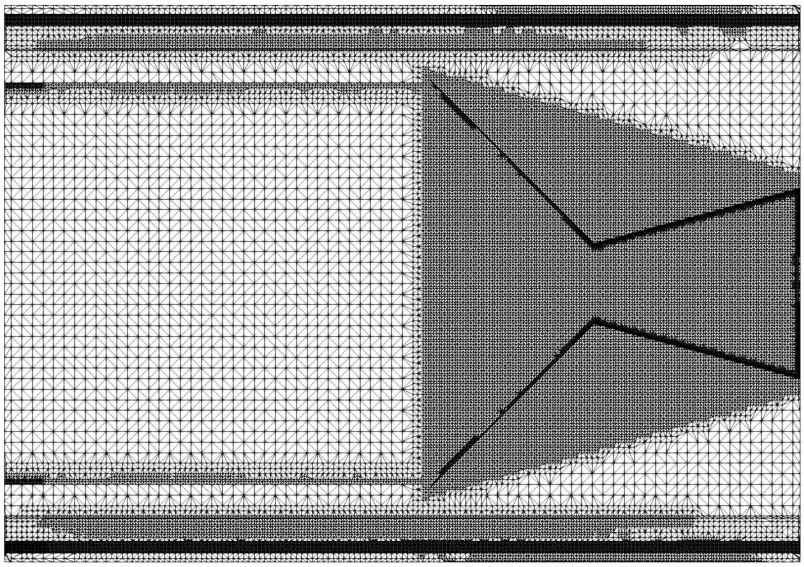

Figure 3.12: Final mesh results including AMR refinement

A full hydrodynamic compressible flow steady state simulation was setup. Steady state was determined by monitoring the temperature of the combustion chamber wall for a steady state value over a minimum of 100 solutions cycles. The solution was initiated with a time step of 0.0001 seconds with the ability to dynamically change based on solution convergence. A density based *Navier-Stokes* solver was used for all solutions.

Turbulence was governed by a *Reynolds-Averages Navier-Stokes* (RANS) equations. a Re-Normalized Group (RNG) $k - \epsilon$ model was implemented to solve the RANS equations. The RNG $k - \epsilon$ solution accounts for fluid flow in small scales of motion. It was found to handle the large variation in fluid scale in this simulation faster when compared to the solution time of others. The *O'Rourke and Amsden* Wall heat transfer model was used for all interfaces in the model.

A base grid of 0.0394 inches (0.001 m) was used globally. The fuel and oxidizer channels were each assigned a starting mesh of the global mesh scaled by three. Similarly the throat area was scaled by 2. Grid scaling was used to shorter the solution time needed. Based on the steady state condition, *Converge CFD* implements a predefined scaling procedure. When a course grid reaches steady state the solver will scale the mesh and use the coarse mesh solution to initialize the finer mesh. Three levels of grid scaling was used. The scaling factors used were 0, 1 and 2.

AMR was implemented in two separate regions. The fluid regions, including the fuel and oxidizer channels and the combustion chamber were allowed to refine up to an additional scaling factor of 4. The velocity was monitored in each region. If convergence was not reached the solver would implement mesh refinement in the specific locations needed while leaving the converged sections course. The combustion chamber/graphite interface and the graphite/stainless steel interfaces were limited at a scaling factor of 3. For these solid surfaces the temperature was monitored for convergence. The initial grid was initialized at a cell count of $17,432$. The final solution was completed at a cell count of 11.2 million.

3.4 Test Setup

Figure 3.13: LRMTS in final configuration prepared for test fire

Extensive work was completed on the LRMTS to allow for safe static firing of the ACMPE engine. The LRMTS was designed and built by the Sierra Nevada Cooperation before being donated to Colorado State University (CSU) in 2016. The LRMTS was originally limited to only testing of solid and hybrid motors. The stand was capable of delivering liquid oxidizer when testing hybrids, but required the motor to have a solid fuel. Prolonged storage required extensive restoration work

in 2022 in order to conduct hybrid testing. Following the restoration an effort was undertaken in 2024 to add liquid fuel capabilities allowing for testing of full liquid engines.

3.4.1 Propellant Delivery

The full plumbing and instrumentation diagram (P&ID) for the test stand can be found in Appendix A. The oxidizer is fed to the engine using inert gas and a intermediate tank. The Oxidizer cylinders are first allowed to equalize with the intermediate tank. Once transfer of oxidizer is complete the fill line is closed and inert gas is used to increase the head space pressure of the tank. The head space pressure is determined before the test based on the expected temperature of the nitrous oxide used for the oxidizer. The nitrous oxide must be pressurized to the point where it will always be in the liquid phase in the intermediate tank.

From the bottom on the oxidizer tank the main feed valve (MFV 1) controls flow to the injector. Immediately after the tank the oxidizer flows through a 2 inch tube. This diameter is gradually decreased to 5/8 immediately before the injector. This continual decrease in tube diameter ensures the oxidizer is unable to expand and vaporize. The inert gas feed line is opened again during firing to maintain constant feed rates.

Similar to the oxidizer the fuel is feed from an intermediate tank using inert gas as a head space pressurant. Loading of the fuel is done as part of the pre test procedures. Being a stable liquid at standard pressure and temperature the fuel can be loaded into the intermediate tank manually by test personal. Once filled, inert gas in introduced to the top of the fuel tank.

Utilizing a dip tube the liquid fuel is pulled from the bottom of the tank. The main feed valve (MFV 2) allows for the flow of fuel to the injector. Due to the stable nature of the fuel and the high pressures of the fluid a constant 3/8 inch diameter tube is used. During testing additional inert gas is fed to the head space of the tank to maintain a constant feed rate. This fuel delivery system was the main focus of the work undertaken. The system was designed, installed and tested.

3.4.2 Data Acquisition and Control Systems

The LRMTS utilizes a National Instruments 9082 CompactRIO (CRIO) for data acquisition and control. The CRIO is housed in a weather proof electronics cabinet located at the front of the LRMTS. An Uninterruptible Power Supply (UPS) provides battery backup for the entire stand in case of power loss (A in figure 3.14).

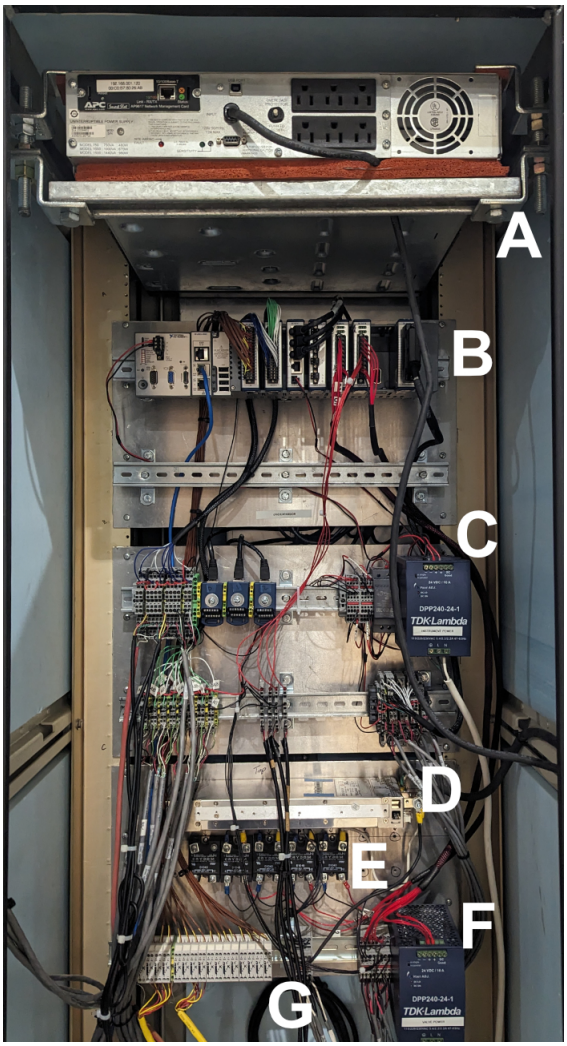

Figure 3.14: Control cabinet

The CRIO (B) is located just below and is connected to the control computer via Ethernet cable. All sensor and control wires are routed though cord grips in the floor of the cabinet to there respective NI modules. Two 10 AMP 24 VDC power supplies (C and D) provide power for the

CRIO and all necessary sensors. High amperage power for ignition is supplied by a 67 AMP, 24 V power supply (D). The high amperage power is controlled via four solid state relays triggered by the CRIO (E). Thermocouple terminal blocks (G) are used to monitor each thermocouple signal for troubleshooting needs.

Eight 0-2,000 PSI pressure transducers are used to monitor and gather data on the LRMTS. Seven K-type thermocouples are used throughout the stand to collect temperature data. Two thermocouples are placed in the intermediate oxidizer tank. One in the head space of the tank and one at the bottom in the fluid. One thermocouple is placed directly upstream of the oxidizer flowmeter. The remainder of the thermocouples are placed on the surface of the engine to record wall temperature during testing. Load cells are used to determine the mass flow rates of each tank. Both tanks utilizes a trio of load cells arranged in a triangular configurations. The pressure transducers and load cells for the fuel delivery system were added through the course of this work. Extensive calibration was undertaken to verify reading on all sensors on the stand.

Table 3.2: Pressure transducers used on the LRMTS

Designator	CRIO Channel	Description
PT 1	Mod 2 AI5	N2 cylinder pressure
PT 2	Mod 2 AI4	Fuel tank pressure
PT 3	Mod 2 AI1	Oxidizer tank pressure
PT 4	Mod 2 AI3	N2O cylinder pressure
PT 5	Mod 2 AI6	Oxidizer injector pressure
PT 6	Mod 2 AI0	Fuel injector pressure
PT 7	Mod 2 AI7	Combustion chamber pressure
PT 8	Mod 2 AI2	Compressed air pressure

The LabVIEW executes in a hierarchical structure where the tasks with higher expediency and operation tasks are prioritized. Reading and processing the signals takes place at 1 kHz. These signals are buffered and recorded at 100 Hz. The automated subroutines are looped at 500 Hz for safety. The user interface is refreshed at a rate of 50 Hz. Four unique data files are saved for each test in the form of TDMS files. The processed sensor data is recorded in *Test Data* while the raw sensor data is recorded in *Raw Data*. The signal sent from the CRIO, either from user input or

from automated subroutines, are recorded in *Logic Data*. The actual position of all valves through the test are recorded in *Position Data*. These four data files provide redundancy in sensor data as well as troubleshooting data in case of stand failure.

Compressed air at 75 PSI (0.52 MPa) is utilized to actuate all pneumatic valves on the stand. Two different pneumatic valves are used on the LRMTS all controlled from the CRIO. The fuel and oxidizer tank vent valves are normally open pneumatically actuated bellows valves. These valves were added during the most recent work in order to meet high safety standards. In case of power failure on the stand these valves will revert to the open position which will allow automatic depressurization of the tanks. The remainder of valves are pneumatically actuated normally closed ball valves. These valves will revert to the closed position in case of power loss.

Several automated subroutines were implemented in this work in the LabVIEW for both safety and timing. The *Abort* sequence interrupts all other sequences and closes all valves on the stand. *Abort All* sequence closes all valves but then initiates a purge and vent sequence. The purge lines are opened (CV 7 and 9). One second later both tanks are vented via CV 2 and 5. After the purge duration specified in the UI, CV 7 and 9 are closed and the lines are vented via CV 8.

Key sensor data is monitored and safe parameters are enforced automatically. If the air compressor pressure falls below 65 PSI (0.45 MPa) the valves could fail to actuate. If this check fails the LabVIEW will automatically disable *Fire* until the pressure has been restored. The pressure in the fuel and oxidizer tanks are monitored for over pressure. At $1,000$ PSI the system will warn the user. If the pressure relief valves fail and in either tank reaches $1,100$ PSI the system will automatically vent the tank in question. The combustion chamber is monitored for over pressurization. If five consecutive pressure readings are above $1,500$ PSI the Abort sequence will be triggered.

The firing sequence starts with a ten second warning countdown. The high amp circuit is then triggered to ignite the pre-burner for a prescribed time. The pre-burner is then allowed to burn for another prescribed delay before both pressurization valves, CV-1 and CV-4 are opened. After a half second delay the oxidizer feed valve, MFV-1 is opened for a half second oxidizer lead. The fuel feed valve, MFV-2 is opened for the set burn time. After this delay the fuel feed line is closed

first providing an additional half second oxidizer lag. Once the oxidizer feed valve has closed both purge lines are immediately opened, CV-7 and CV-9. The purge is run for a prescribed amount of time before closing the valves.

Chapter 4

Results

4.1 Analytical Results

Solving the analytical models described above the quasi-2D temperature profiles were found. The RCST outer surface was found to peak at 2057°F (1125°C). This peak is seen at the inside wall throat. The cooling rate of the radiation is predicted to be approximately 785 BTU/hour (230 Watts). As radiation is the only mode of cooling the outer surface temperature has a dramatic impact on the cooling capacity.

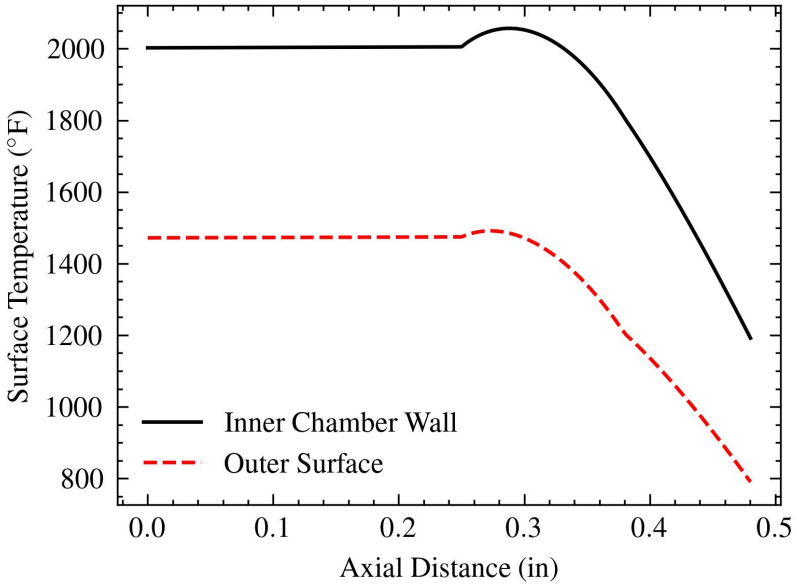

Figure 4.1: Outer and inner steady state surface temperature of the RCST

The outer surface temperature can be controlled by increasing or decreasing the outer radius of the thruster and thus changing the outer surface area. The melting point of the titanium alloy used in this design dictates a maximum operational temperature of $2,912$°F ($1,600$°C). The wall thickness shown in Figure 3.2 was chosen to maximize the surface temperature while retaining a factor of safety and minimizing thruster weight. Due to the simplified design, fast manufacturing

time and low testing costs allowed for rapid prototyping, The analytical model above was deemed sufficient to proceed with testing of the RCST.

In the early stages of the projects it was decided to incorporate a iterative approach to the modeling done on both the RCST and RCMPE platforms. The models were designed using many assumptions on initial conditions, performance and engine behavior. The rapid testing schedule prescribed for both engines provided an iterative approach to refining these assumptions through testing. The testing would allow for more accurate modeling to use on each iteration of the engines.

For to the fast and inexpensive iterations planned for the RCST the analytical model was determined to be satisfactory for the first iteration of the design. Due to the variation in the cooling capacity based on the ambient assumptions made for the radiation cooling, testing was imperative to the refinement of the analytical model. It was decided that for the RCST emphasis should be placed on the testing of the engine to confirm cooling capacity.

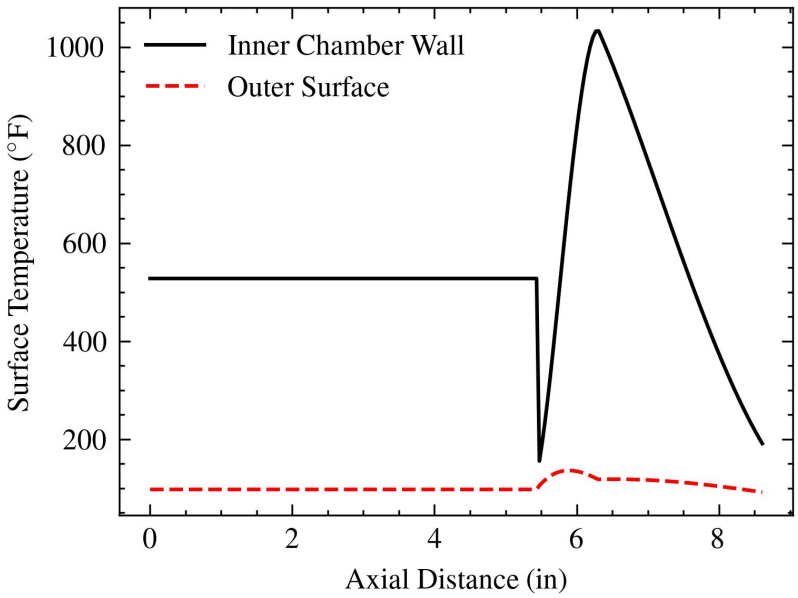

Figure 4.2: Outer surface temperature predicted for the ACMPE

The ACMPE analytical model predicted an outer combustion chamber temperature for steady state firing. Due to the insulation/ablation properties of the combustion chamber liner a very low temperature of 97.6°F (36.4°C) was predicted. A much higher temperature of 136.3°F (57.9°C)

was predicted at the throat where the maximum is expected. This ACMPE results proved to show the limitations of the analytical model used, discussed further later in this chapter.

As explored in Chapter 3, the RCMPE presented the most complex analysis. With several large assumption required to solve the model, as well as dynamic fluid properties a lower confidence was prescribed to the analytical model. Even with the complexities required in the calculations the total run time for the RCMPE model was approximately 30 seconds.

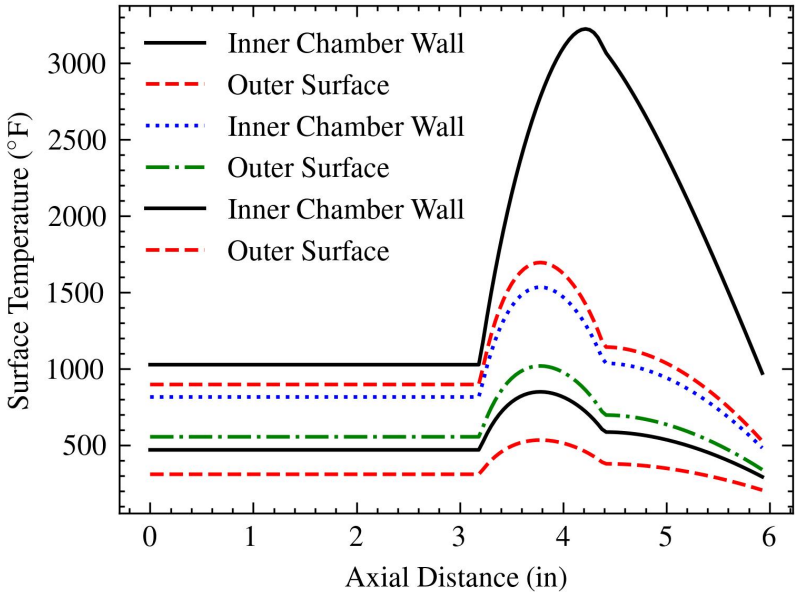

Figure 4.3: Temperature profiles of each node in the resistive circuit analysis of the RCMPE

The model predicted a inner surface temperature of $1,027$°F (552°C) and $3,224$°F ($1,773$°C) for the combustion chamber and throat respectively. The graphite used as the chamber liner while capable of these temperature can be expected to ablate significantly. Additionally the very low thermal conductivity of the graphite restricts heat flow from the combustion chamber to the cooling channels. The outer surface of the engine was predicted to be 309°F (153°C) and 532°F (277°C) for the combustion chamber and throat respectively.

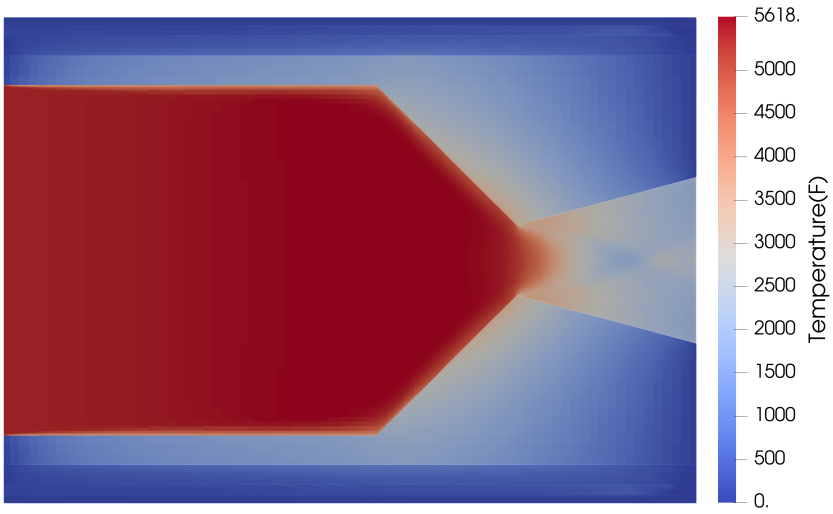

Figure 4.4: 2D Temperature gradient of the RCMPE found using CFD analysis

4.2 Computation Fluid Dynamic Solution Results

The CFD solution while optimized for fast convergence averaged 60 hours per solution. Figure 4.4 represents a 2D plane displaying the temperature from the CFD solution. The coolant channels located at the top and bottom of the image can be seen to be the coolest while the throat is seen to be the hottest.

The main metric of comparison used between the CFD and analytical solutions was the combustion chamber/nozzle inner surface temperature. As the hottest surface in the system, as well as the most simplified in the analytical model, the largest difference was expected in this metric.

The largest variation in models can be seen in the combustion chamber wall temperature ($x = 0$ to $x = 2.95$ inches). Additional variation can be seen past the throat as the nozzle and exhaust gas cools. The largest percent difference between the models is seen at the end of the nozzle at approximately 55%. A miximum difference of 7% can been seen at the throat. The average percent difference over the entire engine is 26%.

Variation can be seen most prominently in the combustion chamber section. This variation can most likely be attributed to the lack of 2D heat transfer in the analytical model. In the case of the CFD solution the higher temperatures at the throat would cause a gradient with the lower

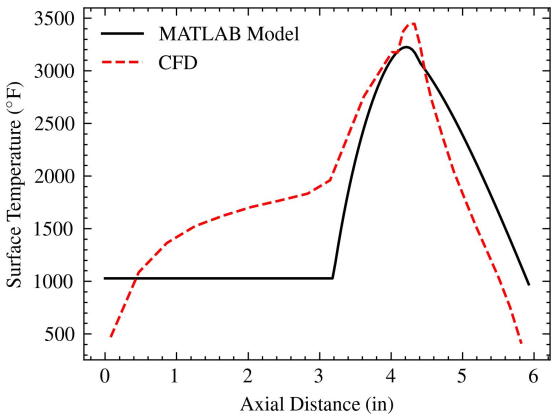

Figure 4.5: Inner surface temperature of both CFD and analytical models

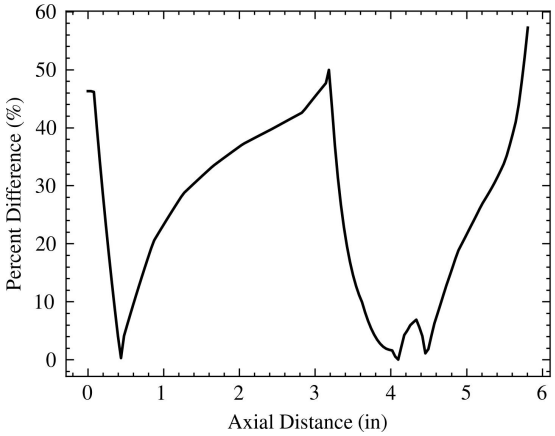

Figure 4.6: Percent difference between CFD and analytical models over the engine length

temperatures near the injector and thus heat transfer would take place in the axial direction. The assumption that all heat transfer takes place in the radial direction excludes the analytical model from taking this phenomenon into account. Very little variation is seen in the throat with areas seeing as little as 1% variation.

One of the goals of this project was to create a simplified model to predict the thermal behavior of various rocket cooling configurations. As evidenced in these results the CFD solution took 60 hours while the simplified analytical model can be solved in under 30 seconds. This significant reduction in solution time shows that the analytical model can be used for fast design iterations to predict the general thermal performance of a variety of rocket engines.

Final solution convergence was monitored by the Turbulant Kinetic Energy (tke) and Energy residuals. Each residual can be plotted and observed. A cyclic behavior can be seen in the tke plot at the end of the simulation. The residual is seen to cycle between 0.0009 and 0.0005. The tke residual can be seen to be more stable although slightly higher. The residual remains fairly constant at approximately 0.09

4.3 Static Fire

Extensive system verification and cold flow testing was completed on the LRMTS before static firing was attempted. System verification included component level reliability testing, control

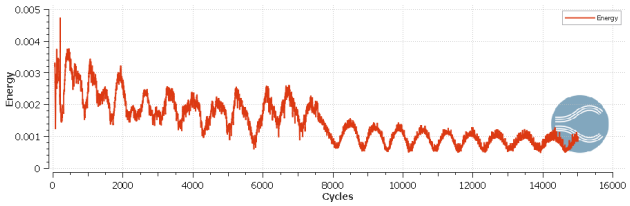

Figure 4.7: Energy residual

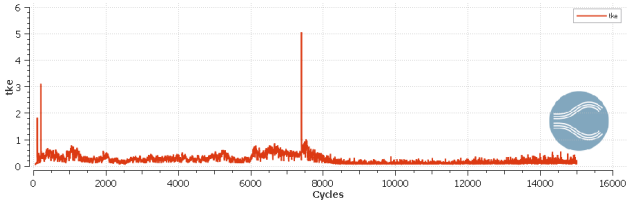

Figure 4.8: tke residual

sequencing tests, and leak testing. Leak testing was conducted on all parts of the system by pressurizing to the operating pressure and waiting one hour (double the expected operating time). The pressure was then monitored and recorded over this hour to verify no noticeable leaks took place.

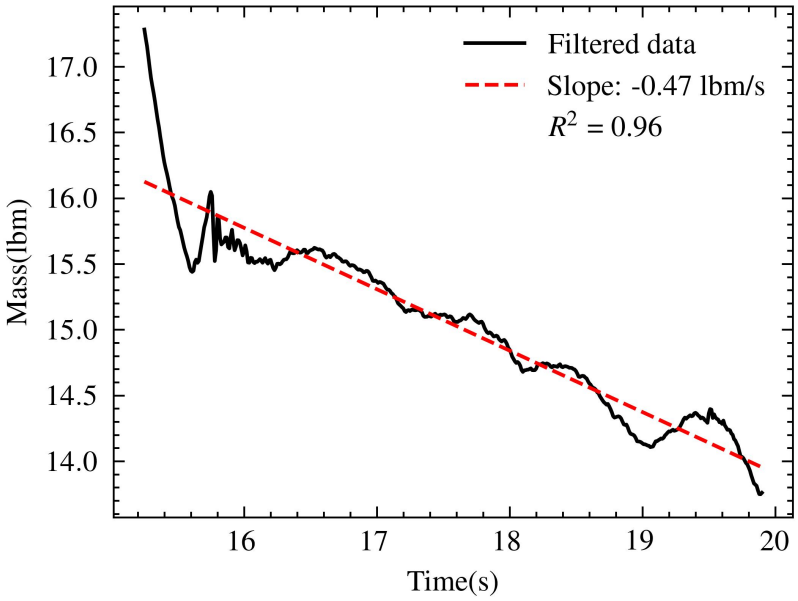

Figure 4.9: Fuel tank mass during cold flow test with alcohol with mass flow rate fit

As flow rates in the ACMPE are controlled by the injector orifices geometry, cold flow testing was used to verify the correct flow rates. Cold flow testing was initially done using water as an

Table 4.1: Cold flow testing results

	Target (lbm/s)	Recorded (lbm/s)	Tolerance (lbm/s)
Fuel	0.52	0.50	0.04
Oxidizer	2.28	2.51	0.24

analogous fluid to the propellant. The Reynolds number was then used to correlate the data to the fuel or oxidizer. With the system proven with water, the propellants (alcohol and nitrous oxide) were loaded on the system and tested independently.

The cold flow tests were conducted using the same procedure as a static fire. The propellant was pressurized to the required pressure using the inert gas feed bottles. The appropriate MFV was then opened for ten seconds in which the water/propellant was allowed to flow through the injector. The mass of the tank was monitored using the load cells during these ten seconds. A linear fit was applied to the mass curve of each test and the slope of this line was used to determine the average mass flow rate for the test. An example mass plot can be seen in Figure 4.9

Through several cold flow test with both alcohol and nitrous oxide, an average flow rate of each was determined. This can be seen in Table 4.1. It is important to note that the tolerance associated with each flow rate are the range of averaged flow rates collected throughout the cold flow campaign and not the actual accuracy of the flow rates. Several issues were identified with the accuracy of the load cell system used to record the tank mass, discussed later.

Static Fire One

With the flow rate verified through cold flow testing the first static fire was conducted. The ambient temperature for the test was approximately $81°$F ($27.2°$C). Figure 4.10 was used to determine the phase of the nitrous oxide for the test. While the ambient temperature at the test condition of 800 PSI indicates a gaseous phase for the nitrous oxide, the tanks were kept cool throughout the test preparation to keep the temperature below saturation point. Additionally, during the filling process the nitrous is expanded resulting in a dramatic chilling of the intermediate tank. The temperature of the nitrous oxide was monitored throughout the entire test and compared to Figure 4.10 to ensure liquid state was maintained. During filling temperature as low as $-58°$F ($-50°$C)

were observed. A maximum injector temperature of 65°F (18°C) was recorded for the duration of the test.

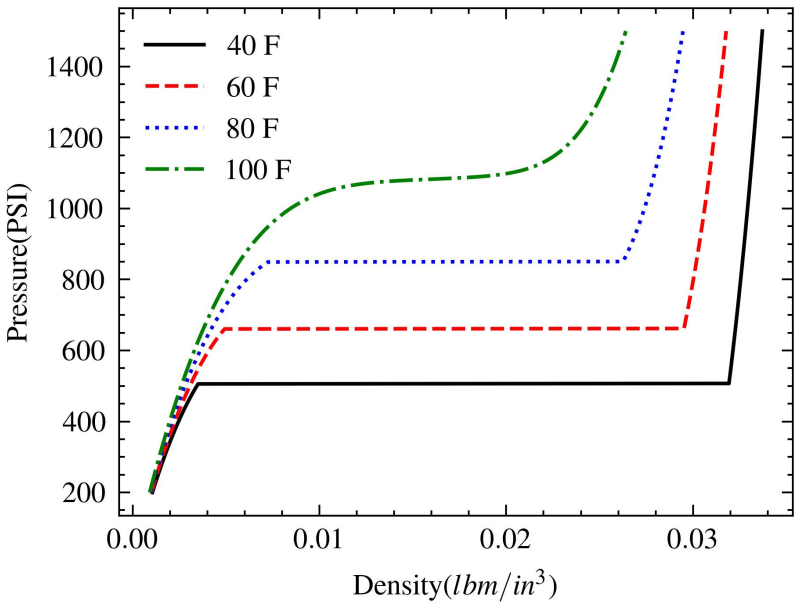

Figure 4.10: Vapor dome of nitrous oxide created by plotting density across wide range of temperature and pressures

The ACMPE was fully assembled and mounted on the LRMTS. The fuel was then loaded manually into the intermediate tank and the stand was armed for firing. The data recording was started and fuel loading commenced. Once fuel was loaded the fire sequence was initiated. Figure 4.11 shows the successful ignition and burning of the preburner.

The automated sequences initiated the propellant flow with a half second oxidizer lead to prevent hard starts. Figure 4.12 shows several frames from the ignition process. It initially appears that the oxidizer flow extinguished the preburner as a large plume of nitrous oxide can be seen exiting the nozzle. Approximately a half second later the oxidizer plume can be seen to ignite and the combustion chamber ignites as well, as the exhaust indicates full engine ignition.

With a successful ignition the test continued to feed propellants to the engine. Approximately one second into the fire, the control computer used for monitoring the test lost connection to the CRIO on the stand. The stand's passive systems designed for such an event successfully terminated

Figure 4.11: The preburner ignited and preheating the combustion chamber before propellants are injected

the test by closing both MFV's and opening the fuel and oxidizer tank vent valves. Due to the loss of connection the control of the valves was lost meaning a manual safe-ing of the stand could not take place. With no smoke or fire present on the engine and stand the tanks vented all propellant in approximately 20 minutes.

Once the stand was deemed safe to approach the physical pressure gauges were checked to verify all pressure had been vented from the system. The loss of connection was determined to be due a power loss to the CRIO. The connection was then re-established by simply restarting the CRIO. The stand safe-ing process was then completed.

Due to the power loss of the CRIO, all recorded data was later found to be corrupted. Several recovery techniques were used in an attempt to recover the data with no success. A screenshot of the front panel on the control panel was captured. The front panel being only for monitoring the test provided minimal data from the test. The pressure history showed no hard start during ignition with a chamber pressure peaking at about 380 PSI (2.6 MPa) and decreasing to a pressure of 336.8 PSI (2.3 MPa) at loss of connection. The thrust was found to follow a similar curve peaking at approximately 310 lbf (1.4 kN) and decreasing to 292.9 lbf (1.3 kN) at connection loss. It was later determined that for this test the pressure scale in Figure 4.14 is not accurate. This was remedied in the front panel and values extracted from Figure 4.14 have been adjusted accordingly.

Figure 4.12: Ignition progression spanning approximately half a second

It was also determined from the front panel data that no significant temperature rise was recorded as the actual fire was too short. The minimal data gathered during this test indicated promising results with the ignition and stability of the engine. Not enough data however was

Figure 4.13: First static fire captured during the one second of operation

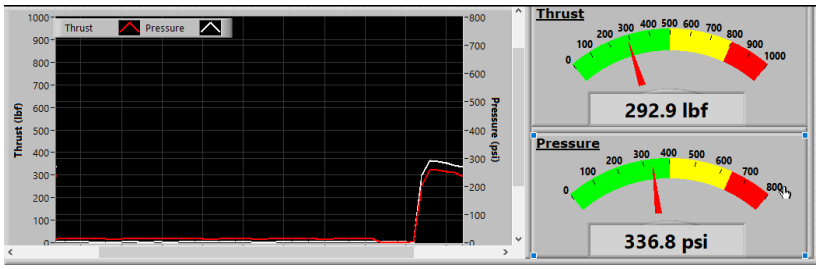

Figure 4.14: Recovered front panel pressure and thrust profile for test one up to connection loss

collected for any extensive analysis of the engine. The engine was therefore disassembled and evaluated for as second test fire. The nozzle and ablative liner were the two components designed to be replaced between test fires. Initial analysis of the nozzle showed very minor wear as seen in Figure 4.16.

The throat is expected to experience the highest temperatures and thus the highest rates of erosion [13]. The nozzle still retained the sharp edges on the converging and diverging side of the throat. No large cracking or chipping was observed from the nozzle so it was determined to reuse the nozzle for a second test fire.

Additionally the ablative liner was measured and no noticeable change in thickness was found from the short burn. The liner was also free from any large crack and the condition was determined to be sufficient for a second test fire. Surface level soot was found on the injector (Figure 4.15). The entirety of the chamber, injection and fittings were cleaned and polished in preparation for

reassembly. The process was documented thoroughly throughout in case of the need for failure analysis.

Figure 4.15: Soot found on the surface of the pintle injector

Figure 4.16: Graphite nozzle condition after first static fire test

Extensive troubleshooting was conducted to detemine the root cause of the power failure. It was determined that a loose screw terminal on a power line for the power supply was the cause of the failure. Rigorous testing was completed to verify the improved wiring would not cause the issue again.

Static Fire Two

The ACMPE was re-assembled and mounted to the LRMTS for the second test fire. The ambient temperature of the day was approximately $85°F$ ($29°C$) and the temperature of the nitrous oxide was closely monitored throughout the test. The test setup procedure was conducted as described in the first static fire. The fire sequence was initiated and successful ignition of the preburner was observed. An almost identical ignition sequence was observed as seen in Figure 4.12. This was expected as no test parameters were changed between the tests.

After ignition the engine continued to burn for the full ten seconds prescribed by the test parameters. The automated sequence successfully shut the engine down with a half second oxidizer lag before immediately open the purge lines to extinguish any remaining flames in the engine. No issues were observed during this test fire and all sensor data was collected.

Figure 4.17: Static fire of the ACMPE on the second static fire test

The thrust recorded can be seen in Figure 4.18 where the grey line represents the target thrust of 650 lbf (2.9 kN). An approximately half second delay can be seen between fuel MFV opening and the generation of thrust. This correlates to the one second delay in ignition seen in Figure 4.12. The first half second can be associated to the oxidizer lead time. A significant drop in thrust can be seen immediately before the closing of the fuel MFV. This can also be seen directly in the combustion chamber pressure in Figure 4.19.

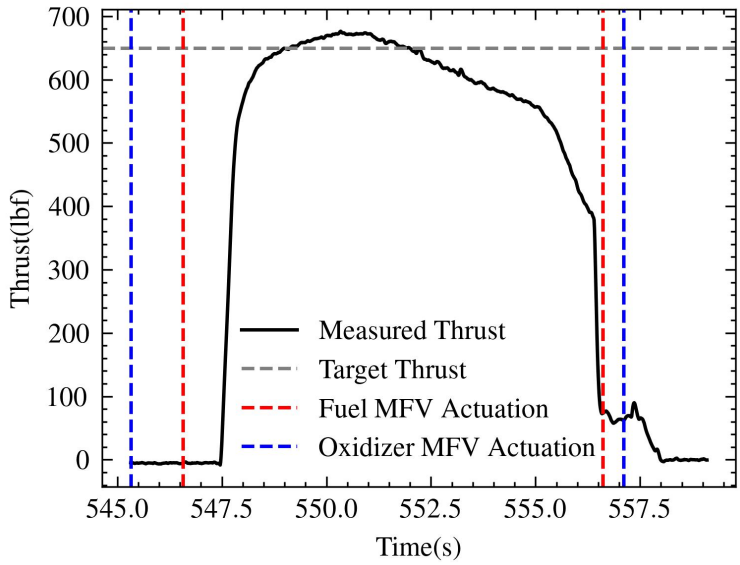

Figure 4.18: Thrust of ACMPE during test duration

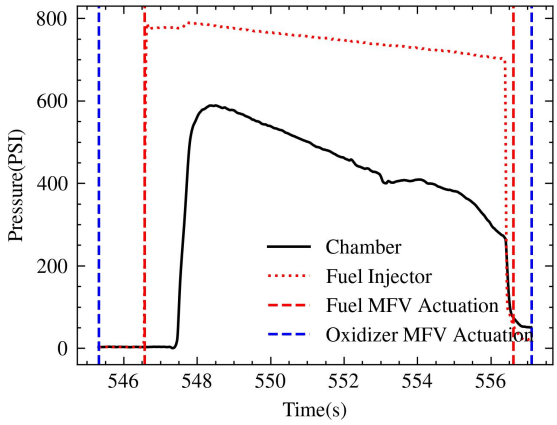

Figure 4.19: Chamber pressure of ACMPE during test duration

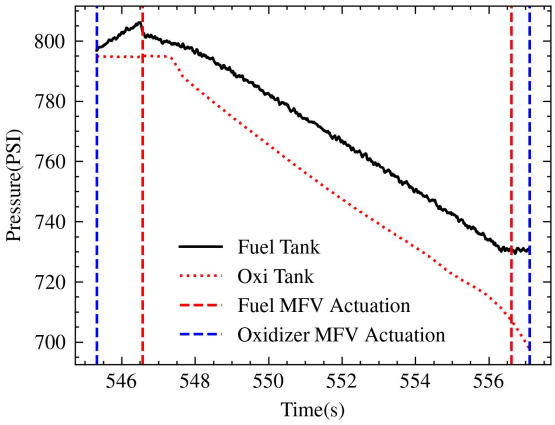

Figure 4.20: Oxidizer and fuel intermediate tank pressures during test duration

The chamber pressure was seen to peak at 588 PSI (4.1 MPa) at ignition. This chamber pressure steadily declined throughout the test duration. The fuel injector pressure can be compared directly to the combustion chamber pressure in Figure 4.19. It can be seen that while the injector pressure also declines steadily over the duration of the burn, the chamber pressure declines at a faster rate.

Sensor failure on the part of the oxidizer injector pressure transducer resulted in no reliable pressure data for the oxidizer injector. Based on cold flow data it can be inferred that the injector pressure can be estimated approximately 30 PSI (0.2 MPa) below that of the intermediate tank pressure. The oxidizer and fuel intermediate tank pressures during the test can be seen in Figure 4.20.

Three k-type thermocouples were surface mounted to the outside of the combustion chamber to monitor the temperature during and after the test. The thermocouples were placed in line with the injector plate, beginning of the converging section of the nozzle and the midway point of the combustion chamber. An immediate heating of the combustion chamber can be seen upon ignition. The nozzle temperature continues to grow as the mid surface and injector temperature begin to taper off.

After engine shutoff the surface temperature continued rising briefly before slightly reducing. At approximately ten seconds after engine shutoff the temperature begins to rise again. Figure

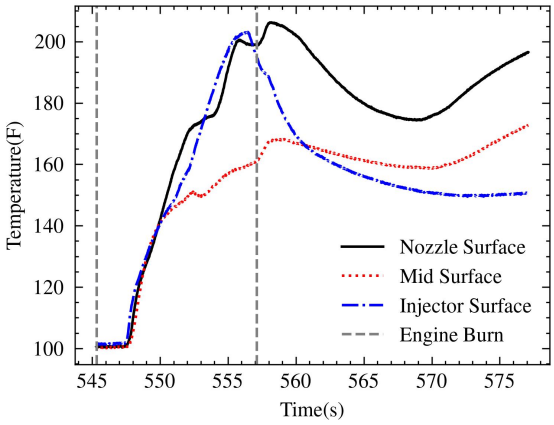

Figure 4.21: Temperature of the combustion chamber surface during the burn duration

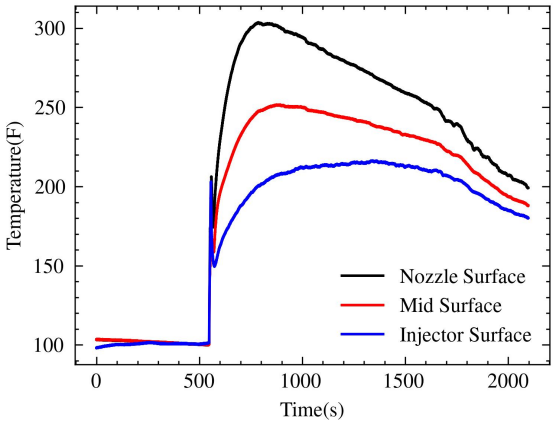

Figure 4.22: Temperature of the combustion chamber surface spanning entire test

4.22 includes the full temperature profile of the surface temperatures. The nozzle surface temperature peaks at 303°F (150°C) approximately three and a half minutes (217 seconds) after engine shutdown. The mid surface peaks at the same time at 251°F (122°C). The injector surface temperature peaks at a later time, approximately thirteen minutes (783 seconds) after engine shutoff. The injector surface peaked at 216°F (102°C).

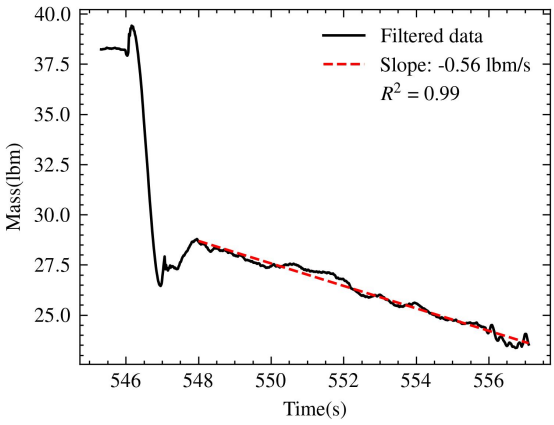

Figure 4.23: Fuel tank mass during fire with mass flow rate linear fit

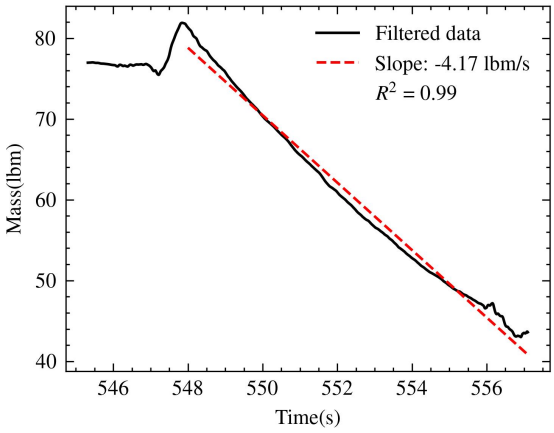

Figure 4.24: Oxidizer tank mass during fire with mass flow rate linear fit

The mass flow rates for each propellant were determined using the load cells placed under the intermediate tanks. Figures 4.23 and 4.24 show the recorded mass data during the duration

of the test. The averaged mass flow rate was determined by a linear line fit. The area of interest for the line fit was specified by the chamber pressure curve to account for the half second delay between the fuel valve opening and ignition of the propellants. That is the averaged mass flow rate calculated by the slope does not take into account the flow rate pre-ignition. The average mass flow rates are 0.56 lbm/s (0.25 kg/s) and 4.17 lbm/s (1.89 kg/s) for the fuel and oxidizer respectively. Both approximations have a calculated R^2 value of 0.99. These average mass flow rates can be used to calculate a 7.4 average oxidizer to fuel ratio for the burn.

The second static fire while initially reaching the target thrust began to drop off in the second half of the burn. The decrease in thrust can be attributed to a number of potential causes. The nozzle was observed to ablate significantly over the course of the static fire. As the nozzle throat ablates the nozzle area increases and thus changes the nozzle geometry. This can have significant effects on the thrust coefficient of the nozzle. Additionally, due to the pressure fed system used to deliver the fuel and oxidizer the injector pressure was seen to drop over the course of the burn. This can be seen in the fuel injector in Figure 4.19.

When comparing the averaged mass flow rates of the fuel and the oxidizer, an oxidizer to fuel ratio of 7.4 was found. This was significantly higher than the expected 4.3. The designed oxidizer to fuel ratio was slightly oxidizer rich while the actual ratio would be very oxidizer rich. This is likely the cause of the higher than expected combustion chamber pressure. The chamber pressure

Figure 4.25: O-ring damage seen on the injector plate

was seen to peak a approximately 600 PSI (4.14 MPa), twice as much as the 300 PSI (2.1 MPa) predicted in the design.

Determining the exact oxidizer to fuel ratio through the burn proved unsuccessful. The oxidizer to fuel ratio of 7.4 was found from the averaged mass flow rates of both the fuel and oxidizer. Significant noise was generated in the load cell signals used to measure the weight of the tanks during the test. Preventative work was done to shorten the signal wire length and ensuring low noise grounds, however these proved insufficient. For safety reasons the static fires took place in an isolated location meaning the power was generated from a gasoline generator. This caused significant signal noise during the test.

The signals were filtered using a *Savitzky-Golay* filter in software to reduce any error before analysis. The noise however was still present in the filtered data to an extent that determining the instantaneous oxidizer to fuel ratio was unsuccessful. The variation in the signal was carried into the oxidizer to fuel ratio resulting in inconsistent values.

During disassembly of the ACMPE, both the injector plate and nozzle were seized inside the combustion chamber. Custom tools were created to extract the injector plate and nozzle. The o-rings on both were seen to be slightly melted and torn in many places. It is undetermined whether the o-ring damage took place during assembly, firing or disassembly.

Significant damage was seen on the ablative liner in the combustion chamber. Approximately 40% of the liner was no longer in place in the combustion chamber. The missing liner pieces were not recovered. Figure 4.26 shows the condition of the liner as it was found upon disassembly. The full amount of liner remaining can be seen in Figure 4.27. No wall damage was seen in sections of the combustion chamber at space where the liner was removed. This indicates the liner failed at the later end of the the test fire. A large amount of liner material was seen to collect on the converging section of the nozzle (Figure 4.28).

The nozzle can be seen to have experienced significant ablation. The previously mentioned straight throat had been completely abraded to a sharp point. Additionally the shape of the throat

Figure 4.26: Combustion chamber liner condition after test fire

Figure 4.27: Combustion chamber liner condition after test fire

was seen to be oval as compared circular throat manufactured. Both these conditions can be seen in Figure 4.29.

The ACMPE showed large variation in the analytical model when compared to the static fire test results. Several factors contributed to these variations most notably the analytical model limitations and non-ideal testing results. The initial project scope included only the RCST and RCMPE. With the termination of the testing campaigns for both engines a third engine was produced based on previous work. The design, mainly the ablative liner and short burn time limited the validation methods. The analytical model developed for the RCST and RCMPE was not designed for modeling ablation or transient conditions.

Due to the method of cooling (ablation) the ACMPE inherently has a limited burn time. The maximum burn time for the ACMPE was designed to be ten seconds and thermal steady state was not achievable during the burn. The analytical model was designed specifically on the assumption of thermal steady state. The test data used to compare to the model were the maximum temper-

Figure 4.28: Liner material collected and melted on the converging section of the nozzle

Figure 4.29: Throat ablation seen in the sharp edge and the non-circularity

atures recorded on the engine surface. This comparison is not perfect and further testing on an engine where thermal equilibrium can be reached is needed.

Additionally as seen in Figures 4.26 and 4.27 significant damage to the liner was observed after the test fire. This damage potentially exposed the bare aluminum to the exhaust gas in the combustion chamber. This would heat the aluminum surface significantly more than the analytical model would predict. Comparing the thermocouple data to the predicted temperatures it can be seen that the analytical model predicts significantly cooler temperatures than recorded in the test fire.

This could be from the missing liner segments that allowed the combustion chamber to heat up or it could be caused by the poor approximations in the analytical model setup. The thermal conductivity of the liner was determined based on published work of similar construction and materials. Slight material differences and construction methods can yield differing thermal conductivity's.

Chapter 5

Conclusion

Modeling the thermal performance of liquid rocket engines is a critical step in the design on novel configurations. Traditional numerical methods such as CFD while very thorough can take days to weeks for each solution. In the fast pace aerospace industry this can severely slow down the initial design process. A modular and fast analytical model is needed to inform early design decisions. Dramatic cost and design time reduction would be seen with a single model capable of predicting thermal performance of numerous steady state cooling configurations.

Through this work an analytical model was created to meet these criteria. The model was capable of a large range of engine size and thrust capabilities. Thermal performance was predicted for both radiative cooling and regenertive cooling. The complex regeneratively cooled engine was compared to a CFD model with promising results. The analytical model was found to solve in under 30 seconds while the CFD model was solved in 60 hours.

Extensive work was completed on the LRMTS to allow for liquid engine testing. The ACMPE was used to verify the test stand functionality. Two successful static fires were completed. While data was not collected for the first static fire, the safety systems implemented worked without issues deeming the static fire a success. Engine performance data was collected from the second static fire to help inform further iterations of all the engines. With the ability to safety and reliably test liquid engines demonstrated, the groundwork was laid to test the RCST and RCMPE.

5.1 Future Work

Further work is needed to fully verify the analytical model created for this project. Testing of the RCST and RCMPE would provide additional data to compare to the analytical and CFD results. As discussed above, test data specifically from an engine capable of thermal equilibrium is needed to validate the analytical model created. Both the RCST and RCMPE were designed for

steady state operation while the ACMPE was not. The ACMPE would need additional cooling and a burn time upwards of half a minute in order to adaquetly compare with the analytical model.

Adding additional capabilities such as ablative modeling and 2D heat transfer would allow for more accurate predictions. Care must be taken to keep the same simplified method when implementing these features as quick solution time is a priority in this model.

Upgrading the data acquisition capabilities of the LRMTS would allow for more accurate and repeatable testing of future rocket engines. Most importantly the addition of mass flow meters can eliminate the need for tank mass measurements to determine mass flow rate. This would not only allow for more precise mass flow rate measurements but would allow for the calculation of the oxidizer to fuel ratio and how it changes over the course of a engine burn. The addition of a high frequency pressure transducer would allow for analysis of combustion instabilities during testing. This is a key metric in validating an engines performance.

In the static fires completed only three thermocouples were available to use for monitoring the surface temperature of the engine. This number should be increased of future testing. Additional thermocouples placed at increments around the circumference of the engine would provide additional data regarding variation in the temperature. In the case of the second static fire additional thermocouples in this configuration would have been able to identify the location where the liner was damaged and determine if that local area experienced additional heating. These additional thermocouples would also allow for redendant measurements.

Bibliography

[1] A. Trejo, M. J. Galvan, A. G. Trujillo, and A. R. Choudhuri, "Experimental investigation of liquid methane convection and boiling in rocket engine cooling channels," in *50th AIAA/ASME/SAE/ASEE Joint Propulsion Conference*, (Cleveland, OH, USA), July 2014.

[2] M. Naraghi, S. Dunn, and D. Coats, "Dual regenerative cooling circuits for liquid rocket engines," in *42nd AIAA/ASME/SAE/ASEE Joint Propulsion Conference & Exhibit*, (Sacramento, CA, USA), July 2006.

[3] L. Browne, "Modeling ablative and regenerative cooling systems for an ethylene ethane nitrous oxide liquid fuel rocket engine," Master's thesis, Colorado State University, 2020.

[4] S. Pravas, "Electric Propulsion – The Future of Space Exploration," 2018. https://www.engineersgarage.com/electric-propulsion-the-future-of-space-exploration/.

[5] G. P. Sutton and O. Biblarz, *Rocket propulsion elements*. Hoboken, N.J: Wiley, 8th ed ed., 2010.

[6] D. K. Huzel, D. H. Huang, and H. Arbit, eds., *Modern engineering for design of liquid-propellant rocket engines*. No. 147 in Progress in astronautics and aeronautics, Washington, DC: American Institute of Aeronautics and Astronautics, rev., updated, and enlarged ed., 1992.

[7] M. Dasilva and N. Hall, "Nozzle Design," *Glenn Research Center | NASA*, 2024.

[8] S. Lee, J. Koo, and Y. Yoon, "Technology and Developing Trends of Pintle Injector for Throttleable Engine," *Journal of the Korean Society of Propulsion Engineers*, vol. 21, no. 4, pp. 107–118, 2017.

[9] C. Greene, R. Woodward, S. Pal, R. Santoro, and R. Garcia, "Design and Study of a LOX/GH2 Throttleable Swirl Injector for Rocket Applications," Jan. 2002.

[10] "A110 a M20 bipropellant, radiatively-cooled thruster for spacecraft attitude control," 2024. https://agilespaceindustries.com/a110.

[11] CEAC, Chemical Analysis and Equilibrium Code, Software Package, NASA, Cleveland, OH, 2005.

[12] G. S. Gill and W. H. Nurick, "Liquid rocket engine injectors," Mar. 1976.

[13] M. Kronwall, "The Development and Implementation of a Hybrid Rocket Motor Thrust Stand to Investigate the Relationship Between Combustion Chamber Pressure and Graphite Rocket Nozzle Erosion in Hybrid Rocket Motors," Master's thesis, Colorado State University, 2022.

[14] "Viscosity - Absolute vs. Kinematic," 2024. https://www.engineeringtoolbox.com/dynamic-absolute-kinematic-viscosity-d412.html.

[15] "Reynolds Number," 2024. https://www.engineeringtoolbox.com/reynolds-number-d237.html.

[16] F. P. Incropera and F. P. Incropera, eds., *Fundamentals of heat and mass transfer*. Hoboken, NJ: John Wiley, 6th ed ed., 2007.

[17] Taler, Dawid and Taler, Jan, "Simple heat transfer correlations for turbulent tube flow," *E3S Web Conf.*, vol. 13, p. 02008, 2017.

[18] M. Rafiee, F. Nitzsche, J. Laliberte, S. Hind, F. Robitaille, and M. R. Labrosse, "Thermal properties of doubly reinforced fiberglass/epoxy composites with graphene nanoplatelets, graphene oxide and reduced-graphene oxide," *Composites Part B: Engineering*, vol. 164, pp. 1–9, May 2019.

Appendix A

Plumbing and Instrumentation Diagram